functionalization of the more electron-deficient arene, whereas the ratio of the initial rates of separate reactions was only 1.2:1 (**11a:1a**). These results suggest that cleavage of the aryl C-H bond is not the overall turnover-limiting step of the silylation of toluene and that the cleavage of the aryl C-H bond of toluene is irreversible.

The regioselectivities of the silylation reactions appear to arise from the steric bulk of both the ligand and the silane. The absence of reactivity with other silanes in the rhodium-catalyzed C–H silylation has prevented a direct comparison of the selectivity of reactions of $HSiMe(OTMS)_2$ with that of other silanes. However, results from the analogous iridium-catalyzed silylations provide evidence for the influence of the silane on the selectivity. The reaction of 5 equivalents of 2-tri(isopropyl)siloxytoluene (**21a**) with Et_3SiH generated the major product in which the silyl group is installed meta to the larger OTIPS group at the less electron-rich position of the arene (82:18 major:minor isomers) (Fig. 4). However, the reaction of 5 equivalents of **21a** with $HSiMe(OTMS)_2$ gave predominantly the product in which the silyl group is installed para to the larger group (7:93 minor:major isomers). We ascribe this change in selectivity to the unfavorable placement of the bulky $SiMe(OTMS)_2$ group meta to the OTIPS group on the arene in the latter transformation.

Conclusions

The intermolecular, rhodium-catalyzed silylation of arenes that we report here occurs under mild conditions, with arene as the limiting reagent and with regioselectivities that complement or surpass those of other arene functionalizations. Several factors lead to the selectivity and synthetic utility of the silylation reaction. First, the silicon reagent is sterically demanding. Assuming the intermediate that cleaves the aryl C–H bond contains a silyl group on the metal, the size of the silane reagent, along with the size of the ancillary ligands, control the degree of regioselectivity. Second, two of the substituents on the silane are bound to silicon through oxygen, and a silicon-heteroatom bond is typically required for many of the transformations of arylsilanes at the C–Si bond. The origin of the remote selectivity remains to be defined. However, our results suggest that a wide scope of functionalization reactions with remote regiocontrol should be achievable through judicious choice of ancillary ligands and reagents with appropriate steric bulk.

References and Notes

1. K. Godula, D. Sames, *Science* **312**, 67–72 (2006).
2. T. W. Lyons, M. S. Sanford, *Chem. Rev.* **110**, 1147–1169 (2010).
3. I. A. I. Mkhalid, J. H. Barnard, T. B. Marder, J. M. Murphy, J. F. Hartwig, *Chem. Rev.* **110**, 890–931 (2010).
4. J. F. Hartwig, *Acc. Chem. Res.* **45**, 864–873 (2012).
5. D. Alberico, M. E. Scott, M. Lautens, *Chem. Rev.* **107**, 174–238 (2007).
6. G. P. McGlacken, L. M. Bateman, *Chem. Soc. Rev.* **38**, 2447–2464 (2009).
7. R. J. Phipps, M. J. Gaunt, *Science* **323**, 1593–1597 (2009).
8. N. Hofmann, L. Ackermann, *J. Am. Chem. Soc.* **135**, 5877–5884 (2013).
9. D. Leow, G. Li, T.-S. Mei, J.-Q. Yu, *Nature* **486**, 518–522 (2012).
10. I. Fleming, J. Dunoguès, R. Smithers, in *Organic Reactions,* A. S. Kende, Ed. (John Wiley & Sons, 1989), vol. 2, pp. 57–193.
11. T.-Y. Luh, S.-T. Liu, in *The Chemistry of Organic Silicon Compounds,* Y. A. Z. Rappoport, Ed. (Wiley, vol. 2, Chichester, 2003), pp. 1793–1868.
12. K. Ezbiansky *et al*., *Organometallics* **17**, 1455–1457 (1998).
13. T. Ishiyama, K. Sato, Y. Nishio, N. Miyaura, *Angew. Chem. Int. Ed.* **42**, 5346–5348 (2003).
14. T. Saiki, Y. Nishio, T. Ishiyama, N. Miyaura, *Organometallics* **25**, 6068–6073 (2006).
15. M. Murata, N. Fukuyama, J.-i. Wada, S. Watanabe, Y. Masuda, *Chem. Lett.* **36**, 910–911 (2007).
16. T. Sakakura, Y. Tokunaga, T. Sodeyama, M. Tanaka, *Chem. Lett.* **16**, 2375–2378 (1987).
17. M. Ishikawa, S. Okazaki, A. Naka, H. Sakamoto, *Organometallics* **11**, 4135–4139 (1992).
18. B. Lu, J. R. Falck, *Angew. Chem. Int. Ed.* **47**, 7508–7510 (2008).
19. H. Ihara, M. Suginome, *J. Am. Chem. Soc.* **131**, 7502–7503 (2009).
20. F. Kakiuchi, K. Igi, M. Matsumoto, N. Chatani, S. Murai, *Chem. Lett.* **30**, 422–423 (2001).
21. J. Oyamada, M. Nishiura, Z. Hou, *Angew. Chem. Int. Ed.* **50**, 10720–10723 (2011).
22. N. A. Williams, Y. Uchimaru, M. Tanaka, *J. Chem. Soc. Chem. Commun.* (11): 1129–1130 (1995).
23. T. Ureshino, T. Yoshida, Y. Kuninobu, K. Takai, *J. Am. Chem. Soc.* **132**, 14324–14326 (2010).
24. Y. Kuninobu, T. Nakahara, H. Takeshima, K. Takai, *Org. Lett.* **15**, 426–428 (2013).
25. E. M. Simmons, J. F. Hartwig, *J. Am. Chem. Soc.* **132**, 17092–17095 (2010).
26. E. M. Simmons, J. F. Hartwig, *Nature* **483**, 70–73 (2012).
27. G. Choi, H. Tsurugi, K. Mashima, *J. Am. Chem. Soc.* **135**, 13149–13161 (2013).
28. C. Cheng, E. M. Simmons, J. F. Hartwig, *Angew. Chem. Int. Ed.* **52**, 8984–8989 (2013).
29. $HSiMe(OTMS)_2$ is commercially available.
30. For applications of phosphine-ligated rhodium catalysts in intramolecular silylation reactions, see (*23*, *24*).
31. Silylcyclohexane [GC–mass spectrometry; mass/charge ratio = 289.1; M-CH_3], from hydrosilylation of the hydrogen acceptor, cyclohexene, is the only major side product.
32. The side reaction, cyclohexene hydrosilylation, consumes both the silane and cyclohexene.
33. For reactions with **8a**, **9a**, and **10a**, the selectivities of silylation meta and ortho to the methoxy groups are 95.4:4.6, 97.0:3.0, and 97.4:2.6, respectively, as determined by GC analysis. The selectivities for all other 1,3-disubstituted arenes are >99:1.
34. T. Ishiyama, Y. Nobuta, J. F. Hartwig, N. Miyaura, *Chem. Commun.* **23**, 2924–2925 (2003).
35. For silylations of **16a** and **17a**, the selectivities for reactions at the 2-positions over all other positions are 98:2 and 97:3, respectively.
36. H. Tajuddin *et al*., *Chem. Sci.* **3**, 3505–3515 (2012).
37. L. T. Ball, G. C. Lloyd-Jones, C. A. Russell, *Science* **337**, 1644–1648 (2012).
38. B. A. Vanchura 2nd *et al*., *Chem. Commun. (Camb.)* **46**, 7724–7726 (2010).
39. Borylation of benzodioxole following the procedure in (*44*) afforded a mixture of meta, ortho, and diborylation products (92% yield) in a ratio of 6:33:61. This difference from (*38*) is likely due to the difference in the amount of the diboron reagent used.
40. Two constitutional isomers of the borylation product, along with a diborylation product, were obtained in a ratio of 43:18:39 following the literature procedure (*44*).
41. E. L. Eliel, S. H. Wilen, L. N. Mander, *Stereochemistry of Organic Compounds* (Wiley, New York, 1994).
42. J. M. Murphy, X. Liao, J. F. Hartwig, *J. Am. Chem. Soc.* **129**, 15434–15435 (2007).
43. S. D. Roughley, A. M. Jordan, *J. Med. Chem.* **54**, 3451–3479 (2011).
44. C. W. Liskey, X. Liao, J. F. Hartwig, *J. Am. Chem. Soc.* **132**, 11389–11391 (2010).

Acknowledgments: We thank the NSF (CHE-1213409) for financial support, Johnson-Matthey for a gift of $[Ir(cod)OMe]_2$, and T. W. Wilson for helpful discussions. A provisional patent application on this work has been submitted.

Supplementary Materials

www.sciencemag.org/content/343/6173/853/suppl/DC1
Materials and Methods
Figs. S1 to S3
Table S1
References (*45*–*58*)

4 November 2013; accepted 14 January 2014
10.1126/science.1248042

Dendritic Inhibition in the Hippocampus Supports Fear Learning

Matthew Lovett-Barron,[1,2]* Patrick Kaifosh,[1,2]* Mazen A. Kheirbek,[2,3] Nathan Danielson,[1,2] Jeffrey D. Zaremba,[1,2] Thomas R. Reardon,[1,2] Gergely F. Turi,[2] René Hen,[1,2,3] Boris V. Zemelman,[4] Attila Losonczy[1,2,5]†

Fear memories guide adaptive behavior in contexts associated with aversive events. The hippocampus forms a neural representation of the context that predicts aversive events. Representations of context incorporate multisensory features of the environment, but must somehow exclude sensory features of the aversive event itself. We investigated this selectivity using cell type–specific imaging and inactivation in hippocampal area CA1 of behaving mice. Aversive stimuli activated CA1 dendrite-targeting interneurons via cholinergic input, leading to inhibition of pyramidal cell distal dendrites receiving aversive sensory excitation from the entorhinal cortex. Inactivating dendrite-targeting interneurons during aversive stimuli increased CA1 pyramidal cell population responses and prevented fear learning. We propose subcortical activation of dendritic inhibition as a mechanism for exclusion of aversive stimuli from hippocampal contextual representations during fear learning.

Aversive stimuli cause animals to associate their environmental context with these experiences, allowing for adaptive defensive behaviors during future exposure to the context. This process of contextual fear conditioning (CFC) is dependent upon the brain

performing two functions in series: first developing a unified representation of the multisensory environmental context (the conditioned stimulus, CS), then associating this CS with the aversive event (unconditioned stimulus, US) for memory storage (*1*–*5*). The CS is encoded by the dorsal hippocampus, whose outputs are subsequently associated with the US through synaptic plasticity in the amygdala (*6*–*10*). The hippocampus must incorporate multisensory features of the environment into a representation of context but, paradoxically, must exclude sensory features during the moment of conditioning, when the primary sensory attribute is the US. The sensory features of the US may disrupt conditioning (*11*). Although the cellular and circuit mechanisms of fear learning and sensory convergence have been extensively studied in the amygdala (*3*, *5*, *12*), much less is known about how the neural circuitry of the hippocampus contributes to fear conditioning.

The primary output neurons of the hippocampus, pyramidal cells (PCs) in area CA1, are driven to spike by proximal dendritic excitation from CA3 and distal dendritic excitation from the entorhinal cortex (*13*). Whereas CA3 stores a unified representation of the multisensory context (*14*), the entorhinal cortex conveys information pertaining to the discrete sensory attributes of the context (*15*). At the cellular level, nonlinear interactions between inputs from CA3 and entorhinal cortex in the dendrites of PCs can result in burst-spiking output and plasticity (*16*–*18*). PCs can carry behaviorally relevant information in the timing of single spikes (*19*), spike rate (*13*), and spike bursts (*20*), but information conveyed with just bursts of spikes is sufficient for hippocampal encoding of context during fear learning (*21*). Distinct CA1 PC firing patterns are under the control of specialized local inhibitory interneurons (*22*, *23*). Whereas spike timing is regulated by parvalbumin-expressing (Pvalb$^+$) interneurons that inhibit the perisomatic region of PCs, burst spiking is regulated by somatostatin-expressing (Som$^+$) interneurons that inhibit PC dendrites (*24*–*26*). This functional dissociation suggests that CA1 Som$^+$ interneurons may play an important role in CFC. However, the activity of specific interneurons during CFC and their causal influence remain unknown.

To facilitate neural recording from multiple genetically and anatomically defined circuit elements in CA1 during CFC with two-photon Ca^{2+} imaging, we developed a variation of CFC for head-fixed mice (hf-CFC). We combined Ca^{2+} imaging with cell-type–specific inactivation tech-

[1]Doctoral Program in Neurobiology and Behavior, Columbia University, New York, NY, USA. [2]Department of Neuroscience, Columbia University, New York, NY, USA. [3]Division of Integrative Neuroscience, New York State Psychiatric Institute, New York, NY, USA. [4]Center for Learning and Memory, University of Texas, Austin, TX, USA. [5]Kavli Institute for Brain Science, Columbia University, New York, NY, USA.

*These authors contributed equally to this work
†Corresponding author. E-mail: al2856@columbia.edu

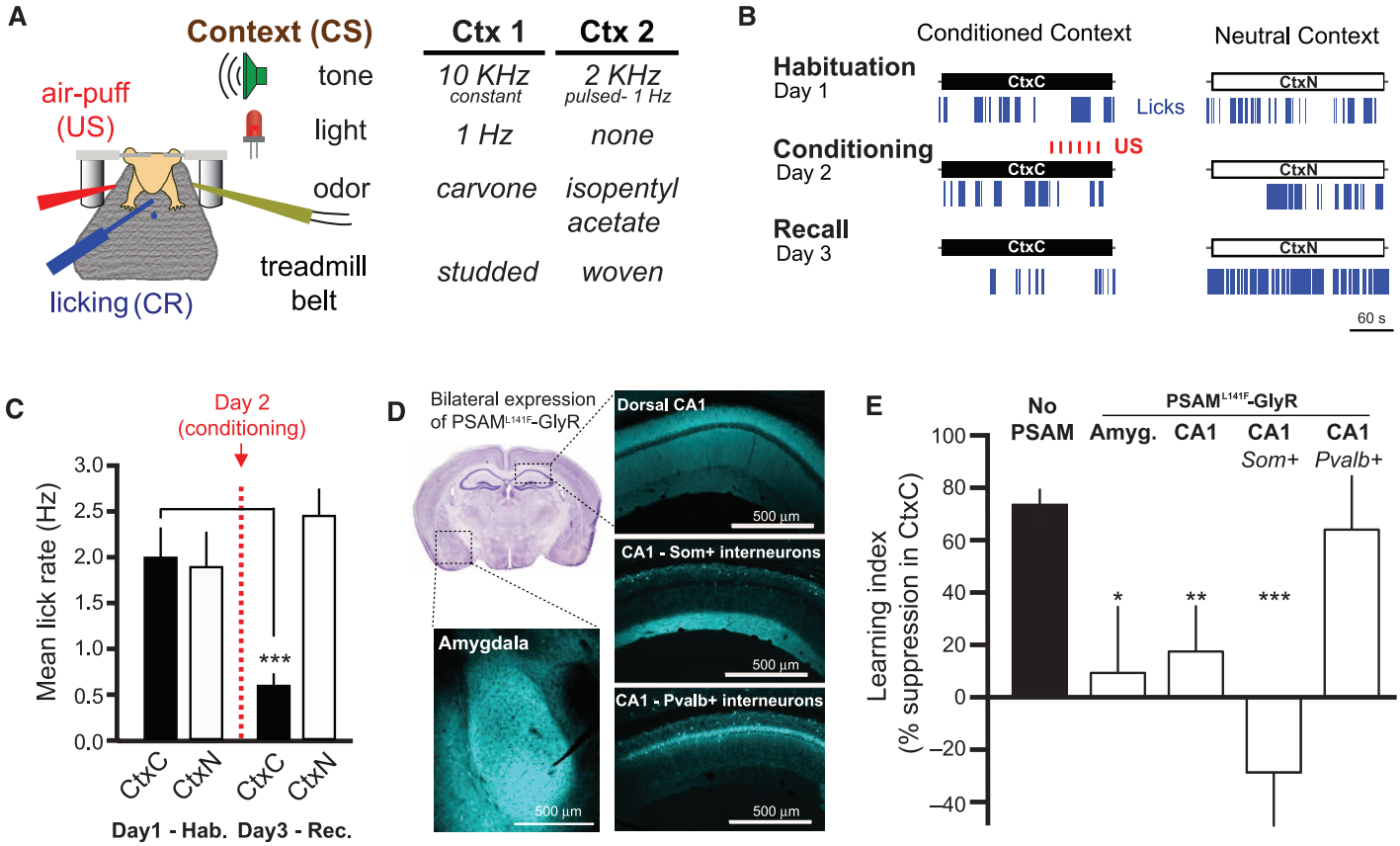

Fig. 1. Som$^+$ interneurons in CA1 are required for learning hf-CFC. (**A**) Schematic of hf-CFC task. A head-fixed mouse on a treadmill is exposed to contexts (CS) defined by distinct sets of multisensory stimuli. We used air puffs as the US and suppression of water-licking as a measure of learned fear (CR). The two distinct contexts used in this study are described at right. (**B**) Behavioral data from an example mouse over the hf-CFC paradigm. Conditioned (CtxC) and neutral (CtxN) contexts are each presented once a day, and lick rate is assessed during the 3-min context. (**C**) Summary data for 19 mice [two-way analysis of variance (ANOVA), context x session, $F_{(1,19)} = 9.34$, $P < 0.01$]. Mice showed a selective decrease in mean lick rate between habituation and recall in CtxC but not CtxN (paired sign tests). (**D**) Viral expression of PSAM^{L141F}-GlyR in the amygdala or dorsal CA1, revealed by α-bungarotoxin-Alexa647 immunostaining. All injections were bilateral; for simplicity, only one hemisphere is shown. Image at top left is from the Allen Brain Atlas. (**E**) Summary data for mice injected with PSEM^{89} systemically 15 min before the conditioning session in CtxC (day 2 of hf-CFC paradigm). Learning is assessed by the percentage of lick-rate decrease in the CtxC recall session (day 3) relative to the mean lick rate in all sessions. Mice expressing PSAM^{L141F}-GlyR in amygdala cells (Amyg., $n = 6$ mice), dorsal CA1 cells (CA1, $n = 5$ mice), or CA1 Som$^+$ interneurons (CA1-Som$^+$, $n = 8$ mice) showed impaired learning compared with mice not expressing PSAM^{L141F}-GlyR (No PSAM, $n = 11$ mice), whereas mice expressing PSAM^{L141F}-GlyR in CA1 Pvalb$^+$ interneurons (CA1-Pvalb$^+$, $n = 4$ mice) did not. Comparisons are Mann-Whitney U tests. Error bars, mean ± SEM. *$P < 0.05$; **$P < 0.01$; ***$P < 0.001$.

niques in head-fixed and freely moving mice to investigate the contribution of CA1 neural circuitry to fear learning.

CFC for Head-Fixed Mice

Conditioned fear in rodents is typically measured in terms of freezing upon re-exposure to the context where the subject experienced an aversive stimulus (*3*, *5*). However, using freezing as a conditioned response (CR) is problematic in head-fixed mice. Instead, we measured learned fear using conditioned suppression of water licking (*27*, *28*), an established measure of fear that translates well to head-fixed preparations. We trained water-restricted mice to lick for small water rewards while head-fixed on a treadmill (*29*), then exposed them to two multisensory contexts (sets of auditory, visual, olfactory, and tactile cues) over three consecutive days and monitored their rate of licking (Fig. 1A and fig. S1A) (see Materials and Methods). On the second day, we paired the air-puff US with one of the contexts and assessed lick rate in both contexts the following day. We found that US pairing caused a decrease in the rate of licking in the conditioned context (CtxC) but not the neutral (CtxN) (Fig. 1, B and C, and fig. S1, B to E).

We used pharmacogenetic neuronal inactivation to test the necessity of the hippocampus and amygdala for the encoding of hf-CFC. We targeted bilateral injections of recombinant adeno-associated virus [rAAV(*Synapsin-PSAM^{L141F}-GlyR*)] to express the ligand-gated Cl^- channel PSAM^{L141F}-GlyR in either dorsal hippocampal area CA1 or the amygdala in wild-type mice (Fig. 1D). Neurons expressing PSAM^{L141F}-GlyR are inactivated for ~15 to 20 min upon systemic administration of its ligand PSEM^{89} (60 mg per kg of weight, intraperitoneally) (*30*). We administered PSEM^{89} to mice before conditioning in CtxC, and tested their memory 24 hours later without the drug by assessing lick suppression in CtxC recall compared with mean licking across all sessions. In agreement with conventional freely moving CFC results (*6*, *7*, *31*, *32*), we found that inactivating neurons in dorsal CA1 or the amygdala prevented contextual fear learning (Fig. 1E).

Som$^+$ Interneurons Are Required for CFC

To determine the relevance of CA1 inhibitory circuits for the acquisition of hf-CFC, we asked whether acute inactivation of γ–aminobutyric acid-releasing (GABAergic) interneuron subclasses in CA1 would alter learning. We injected rAAV (*Synapsin-PSAM^{L141F}-GlyR*)^{cre} bilaterally into CA1 of *Som-cre* or *Pvalb-cre* mice to express PSAM^{L141F}-GlyR selectively in either Som$^+$ dendrite-targeting

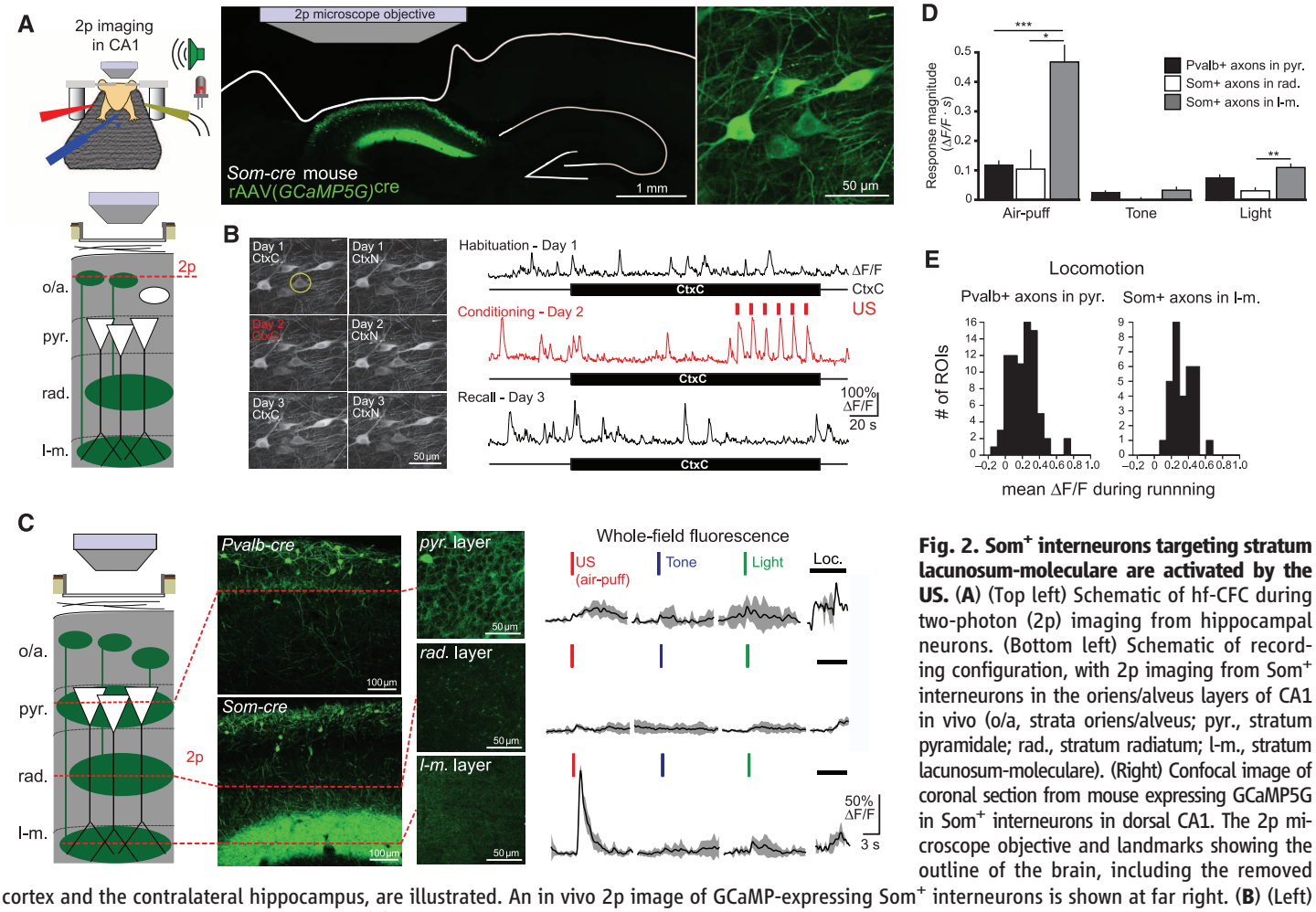

Fig. 2. Som$^+$ interneurons targeting stratum lacunosum-moleculare are activated by the US. (**A**) (Top left) Schematic of hf-CFC during two-photon (2p) imaging from hippocampal neurons. (Bottom left) Schematic of recording configuration, with 2p imaging from Som$^+$ interneurons in the oriens/alveus layers of CA1 in vivo (o/a, strata oriens/alveus; pyr., stratum pyramidale; rad., stratum radiatum; l-m., stratum lacunosum-moleculare). (Right) Confocal image of coronal section from mouse expressing GCaMP5G in Som$^+$ interneurons in dorsal CA1. The 2p microscope objective and landmarks showing the outline of the brain, including the removed cortex and the contralateral hippocampus, are illustrated. An in vivo 2p image of GCaMP-expressing Som$^+$ interneurons is shown at far right. (**B**) (Left) 2p images of the same field of view from (A) for the six hf-CFC sessions over the course of 3 days. Images are time averages of 2000 motion-corrected imaging frames collected for each imaging session. (Right) $\Delta F/F$ traces from an example Som$^+$ CA1 interneuron (circled at left) over the three daily exposures to CtxC. (**C**) (Left) Schematic of recording configuration, with in vivo 2p imaging from Som$^+$ axons in radiatum or lacunosum-moleculare layers of CA1, Pvalb$^+$ axons in the pyramidale layer. (Middle) Expression of GCaMP5G in layer-specific axonal projections, revealed by confocal images of coronal sections and in vivo 2p images of each layer. (Right) Example trial-averaged responses (five trials each presented in pseudorandom order) of layer-specific whole-field fluorescence responses to discrete 200-ms sensory stimuli and locomotion (mean with shaded SD). (**D**) Summary data for sensory stimulation experiments shown in (C). Responses are quantified as the mean integral of whole-field $\Delta F/F$ over the 3 s after the stimulus. [two-way ANOVA, axon-type x stimulus type, $F_{(4,84)} = 16.9$, $P < 0.001$; post hoc Mann-Whitney U tests]. Error bars, mean ± SEM. *$P < 0.05$; **$P < 0.01$; ***$P < 0.001$. (**E**) Summary data for whole-field $\Delta F/F$ responses to treadmill-running. Pvalb$^+$ axons in pyramidale exhibit locomotion responses similar to Som$^+$ axons in lacunosum-moleculare (Mann-Whitney U test, $P = 0.101$).

interneurons or Pvalb$^+$ perisomatic-targeting interneurons, respectively (*25*) (Fig. 1D and fig. S2). Systemic PSEM^{89} administration during conditioning prevented learning in mice expressing PSAM^{L141F}-GlyR in CA1 Som$^+$ interneurons, but not in mice expressing PSAM^{L141F}-GlyR in CA1 Pvalb$^+$ interneurons (Fig. 1E).

We repeated our inactivation experiments in conventional CFC experiments with freely-moving mice, with a foot-shock US and freezing as the CR. Inactivating CA1 Som$^+$ interneurons during conditioning prevented recall 24 hours later without the drug, while inactivating Pvalb$^+$ interneurons had no effect (fig. S3, A and B). Inactivating Som$^+$ interneurons or Pvalb$^+$ interneurons did not alter perception of the US, as hippocampal-independent auditory cued conditioning was left intact (fig. S3C). Inactivating Som$^+$ neurons did not simply alter CS perception, as inactivation during both conditioning and recall also prevented learning (fig. S4). The absence of a role for Pvalb$^+$ interneurons in CFC was not due to insufficient neuronal inactivation. In agreement with previous findings (*33*), this manipulation reduced performance in a spatial working memory task (fig. S5).

The US Activates Som$^+$ Interneurons

We used two-photon Ca^{2+} imaging to record the activity of CA1 Som$^+$ interneurons over the course of hf-CFC. We unilaterally injected rAAV(*Synapsin-GCaMP5G*)^{cre} into dorsal CA1 of *Som-cre* mice to express the genetically encoded Ca^{2+} indicator GCaMP5G (*34*) in the somata, dendrites, and axons of Som$^+$ interneurons (Fig. 2A). To visualize CA1 neurons in vivo, we used established surgical techniques (*29*, *35*) to implant a chronic imaging window superficial to dorsal CA1. After recovery, water restriction, and habituation to head-restraint, we engaged mice in the hf-CFC task while imaging Ca^{2+}-evoked GCaMP5G fluorescence transients from Som$^+$ interneuron somata in the oriens and alveus layers of CA1. We returned to the same field of view for each of the six sessions of hf-CFC (Fig. 2B) and processed fluorescence time-series data using established methods for motion-correction and signal processing (*29*, *36*). Strikingly, Som$^+$ interneurons displayed increased activity in response to the US during hf-CFC (example neuron in Fig. 2B).

To investigate the dynamics of stimulus-evoked GABAergic signaling in more detail, we imaged CA1 inhibitory neurons during the pseudorandom presentation of discrete sensory stimuli from the hf-CFC task: light flashes and tones, which were elements of the CS, or air-puffs, which served as the US. To image a greater variety of interneurons simultaneously, we injected cre-independent rAAV(*Synapsin-GCaMP5G*) into CA1 of *Som-cre* mice crossed with a tdTomato reporter line, which allowed us to simultaneously image sensory responses of Som$^+$ and Som$^-$ interneurons (fig. S6A). Air puffs activated most Som$^+$ interneurons (fig. S6B), whereas a smaller proportion of Som$^-$ and Pvalb$^+$ interneurons had comparable responses (fig. S6C).

Not all Som$^+$ interneurons were activated by the air puff, which could reflect a difference between bistratified cells and oriens-lacunosum-moleculare (OLM) cells, both of which are labeled in *Som-cre* mice (*25*). The axons of bistratified cells arborize in stratum oriens and radiatum, whereas those of OLM cells arborize in stratum lacunosum-moleculare (*22*, *23*). These two inhibitory projections contact the dendritic compartments of CA1 PCs that receive input from CA3 and the entorhinal cortex, respectively, suggesting potentially distinct functions. To isolate the relative contributions of these two inhibitory pathways to US-evoked signaling, we labeled Som$^+$ neurons with GCaMP5G in *Som-cre* mice and focused our imaging plane on the axons of bistratified cells in radiatum, or the axons of OLM cells in lacunosum-moleculare (Fig. 2C).

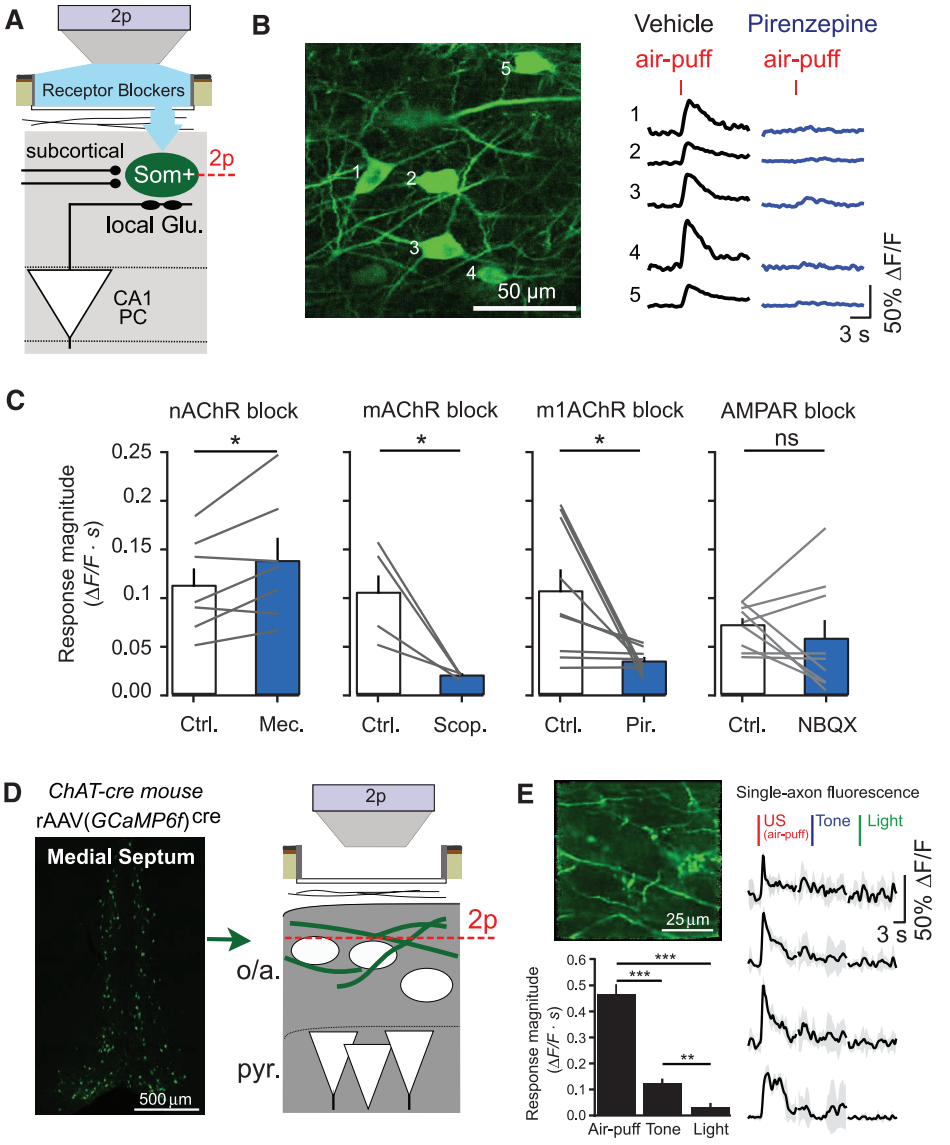

Fig. 3. Cholinergic inputs from the medial septum drive CA1 Som$^+$ interneurons during the US. (**A**) Schematic of recording configuration, with 2p imaging from Som$^+$ interneurons in the oriens and alveus layers of CA1, and local pharmacological manipulations through an aperture in the imaging window. (**B**) Example in vivo 2p image of GCaMP-expressing Som$^+$ interneurons and their fluorescence responses to air puffs in vehicle (cortex buffer) and in the presence of 1 mM pirenzepine. (**C**) Summary data for local pharmacological manipulations. Each point is the mean response of all Som$^+$ interneurons within a field of view (FOV) to air puffs (5 trials each) in vehicle (Ctrl.) and upon drug application (nAChR block, 7 FOVs in 5 mice; mAChR block, 4 FOVs in 3 mice; m1AChR block, 9 FOVs in 5 mice; AMPAR block, 9 FOVs in 4 mice). Comparisons are paired *t* tests between drug conditions. (**D**) (Left) Coronal confocal image of GCaMP6f$^+$/ChAT$^+$ neurons in the medial septum of a *ChAT-cre* mouse. (Right) Schematic of recording configuration, with 2p imaging from ChAT$^+$ axons in the oriens and alveus layers of CA1. (**E**) (Top left) Example in vivo 2p image of GCaMP6f-expressing ChAT$^+$ axons in CA1. (Right) Mean responses of individual axons to sensory stimuli. (Bottom left) Summary data from ChAT$^+$ axons averaged within each FOV (sign tests; n = 20 FOVs in 2 mice). Error bars, mean ± SEM. *P < 0.05; **P < 0.01; ***P < 0.001; ns, nonsignificant.

Whole-field recording from the dense Som$^+$ axonal termination in lacunosum-moleculare revealed a fast, high-amplitude increase in fluorescence in response to the air puff but not the tone or light (Fig. 2D). In contrast, the lower density axons in radiatum revealed little response to these stimuli. We also expressed GCaMP5G in *Pvalb-cre* mice to record from Pvalb$^+$ basket cell axons in stratum pyramidale. These high-density axons had much smaller responses to the US (Fig. 2, C and D) but responded robustly to treadmill running (Fig. 2E).

Acetylcholine Drives Som$^+$ Interneurons

To drive fast-onset responses to the US, Som$^+$ interneurons in CA1 must receive a time-locked source of US-driven excitation. However, most excitatory inputs to OLM cells are synapses from CA1 PCs (*23*), and PCs do not encode the US (*5*, *10*) or robustly respond to it (fig. S6C) (*37*–*40*). Alternatively, Som$^+$ interneurons could be excited by extrahippocampal sources such as subcortical neuromodulatory inputs. Indeed, OLM cells in CA1 can be depolarized through both nicotinic and muscarinic acetylcholine receptors (*41*, *42*), and lesions of cholinergic inputs from the medial septum are known to prevent the suppressive effects of aversive stimuli on CA1 spiking activity (*38*, *43*–*45*). Additionally, neocortical interneurons have been demonstrated to respond to aversive stimuli through cholinergic input (*46*).

To probe the source of US-evoked activation of Som$^+$ interneurons, we modified our imaging window to allow for local pharmacological manipulation of the imaged neural tissue (fig. S7A) (*29*). We applied antagonists of neuromodulatory receptors through the imaging window, which passively diffused into CA1; there, we imaged GCaMP5G-expressing Som$^+$ interneuron responses to stimuli before and after drug administration (Fig. 3, A and B). Blockade of the nicotinic acetylcholine receptor (nAChR) did not decrease Som$^+$ interneuron responses to air puffs (1 mM mecamylamine) (Fig. 3C) but instead modestly increased responses. However, blockade of the muscarinic acetylcholine receptor (mAChR) significantly reduced air-puff responses in Som$^+$ interneurons (1 mM scopolamine) (Fig. 3C). We recapitulated this result with more selective blockade of type 1 mAChRs (1 mM pirenzepine; Fig. 3, B and C), which reduced air-puff–evoked Som$^+$ interneuron responses in a dose-dependent manner (fig. S7B). Metabotropic receptors like mAChRs generally act on slower time scales, but studies in brain slices have demonstrated that muscarinic input can evoke fast-onset depolarization and spiking of CA1 OLM cells (*41*, *47*). mAChRs in dorsal hippocampus are required for encoding CFC (*48*), and our results suggest a possible circuit mechanism that contributes to this requirement. This effect was not a consequence of reduced disynaptic drive from m1AChR-responsive PCs (*49*), because m1AChR block did not substantially alter air-puff–evoked activity in the minority of responding PCs (fig. S7C), and responses of Som$^+$ interneurons were not substantially changed by blockade of glutamatergic AMPA receptors (20 μM 2,3-Dioxo-6-nitro-1,2,3,4-tetrahydrobenzo[*f*]quinoxaline-7-sulfonamide) (Fig. 3C).

Cholinergic input to the hippocampus arises from projection neurons in the medial septum (*50*), a region required for CFC (*51*). To directly record the activity of these projections, we injected rAAV(*ef1α-DIO-GCaMP6f*)^{cre} into the medial septum (MS) of *ChAT-cre* mice to express the sensitive Ca^{2+} indicator GCaMP6f (*52*) in cholinergic projection neurons. We imaged cholinergic (ChAT$^+$) axons in the oriens and alveus layers of CA1 during sensory stimulation (Fig. 3D and fig. S8). ChAT$^+$ axons responded robustly to air puffs, with smaller responses to tones and very little response to light flashes (Fig. 3E). ChAT$^+$ axon responses were independent of air-puff duration, similar to Som$^+$ axons in lacunosum-moleculare (fig. S9) but differing from the graded responses of septohippocampal GABAergic projections (*29*).

Coaligned Dendritic Inhibition and Excitation

The distal tuft dendrites of PCs receive excitatory input from the entorhinal cortex, raising the possibility that the inhibition we observe is counteracting US-evoked excitation to these dendrites. The entorhinal cortex provides sensory information to CA1 (*15*), including projections from the lateral entorhinal cortex (LEC) (*53*) and nonspatial neurons of the medial entorhinal cortex (MEC) (*54*) that synapse with CA1 PC distal dendrites. In contrast, the proximal dendrites of PCs receive input from CA3 believed to carry stored contextual representations rather than sensory information (*14*). To directly record from these excitatory inputs, we injected rAAV(*Synapsin-GCaMP6f*) into CA3, LEC, or MEC and imaged axonal activity in ipsilateral CA1 layers oriens/radiatum (CA3 axons) or lacunosum-moleculare (LEC and MEC axons) (Fig. 4A and fig. S10, A and B). Sensory inputs, particularly aversive air puffs, evoked stronger signals from LEC and MEC axonal boutons compared with CA3 axonal boutons, reflected by changes in whole-field fluorescence (Fig. 4, B and C). These data indicate that US-driven inhibition of PC distal tuft dendrites in stratum lacunosum-moleculare is coaligned with

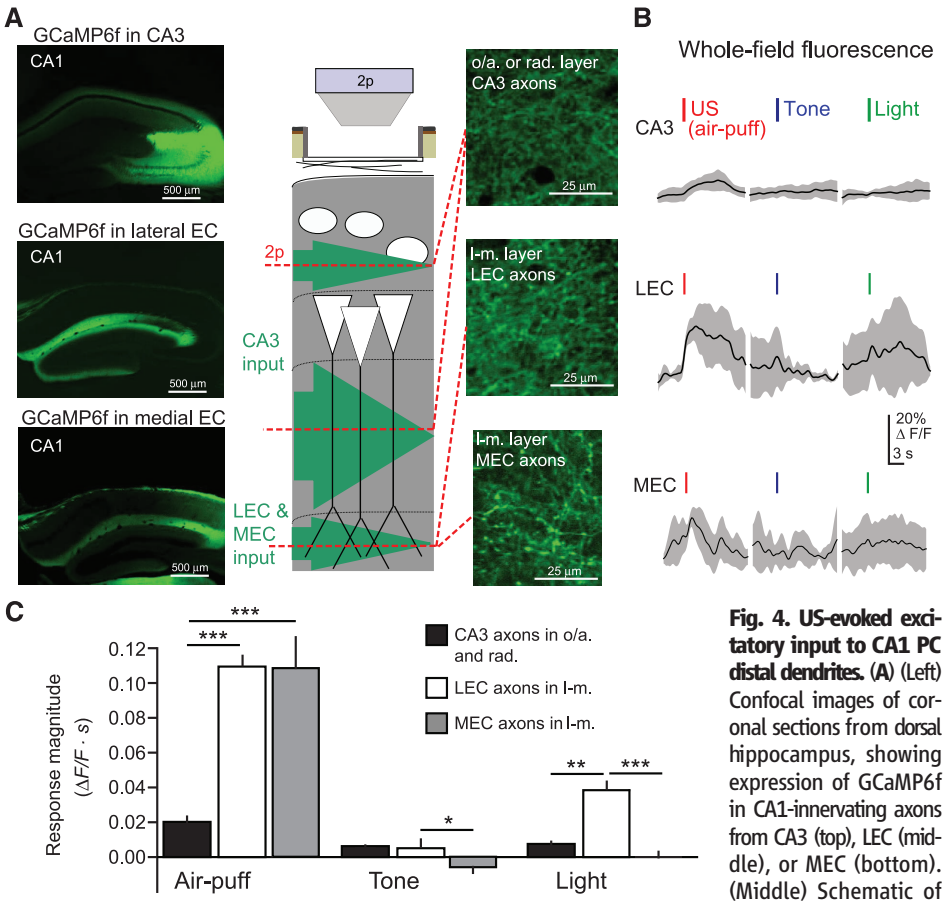

Fig. 4. US-evoked excitatory input to CA1 PC distal dendrites. (A) (Left) Confocal images of coronal sections from dorsal hippocampus, showing expression of GCaMP6f in CA1-innervating axons from CA3 (top), LEC (middle), or MEC (bottom). (Middle) Schematic of recording configuration, with 2p imaging from excitatory axons in the oriens/radiatum layers (CA3 projections) or lacunosum-moleculare layer (LEC or MEC projections) of CA1. (Right) Example in vivo 2p images of GCaMP6f-expressing axons in CA1 (CA3, top; LEC, middle; MEC, bottom). **(B)** Example mean whole-field fluorescence traces from CA3, LEC, and MEC axons [examples in (A)], in response to discrete sensory stimuli (mean with shaded SD). **(C)** Summary data for sensory stimulation experiments. Responses are quantified as the mean integral of $\Delta F/F$ over the 3 s after the stimulus (two-way ANOVA, axon type x stimulus type, $F_{(4,84)} = 10.7$, $P < 0.001$; post hoc Mann-Whitney U tests). Error bars, mean ± SEM. *$P < 0.05$; **$P < 0.01$; ***$P < 0.001$.

excitatory input, which could effectively limit dendritic depolarization (*55*). Compartmentalized inhibition can also prevent propagation of excitation from distal to proximal dendrites (*16*–*18*), potentially preserving responses of PCs to sparse excitation from CA3 axons (fig. S10C). Similar US-driven signals may occur in other excitatory inputs to lacunosum-moleculare, such as the thalamic reuniens nucleus.

Consequences for Hippocampal Output and Learning

Ultimately, any dysfunction in hippocampal encoding of context is likely reflected in changes to the primary hippocampal output neurons: CA1 PCs. Som$^+$ interneurons appear poised to inhibit excitation during the US and are required for CFC, but the response of PCs in their absence is unknown. To probe the consequences of inactivating Som$^+$ interneurons for US-evoked PC population activity, we simultaneously imaged air-puff responses of ~150 to 200 PCs while inactivating Som$^+$ interneurons. We injected rAAV(*Synapsin-PSAM^{L141F}-GlyR*)^{cre} and rAAV(*Synapsin-GCaMP6f*) into CA1 of *Som-cre* mice, and imaged air-puff–evoked responses of PC populations in pyramidale before and during Som$^+$ interneuron inactivation with local application of PSEM^{89} through the hippocampal imaging window (Fig. 5A). Although systemic PSEM^{89} reduced air-puff–evoked Ca^{2+} activity in Som$^+$/PSAM^{L141F}GlyR$^+$ interneurons (fig. S11), we applied PSEM^{89} locally to the imaging window to extend the duration of neuronal inactivation. We imaged PC populations during control conditions and PSEM^{89} application, identifying neurons with significant air-puff–evoked Ca^{2+} transients (fig. S12) (*36*). Inactivating Som$^+$ interneurons significantly increased the number of PCs activated by the air puff within a field of view (Fig. 5, B and C) and significantly increased the duration of Ca^{2+} transients in PCs that responded to the US in both control and PSEM^{89} conditions (Fig. 5, B and C). Extended transient duration likely corresponds to the longer spike bursts previously reported from electrophysiological measurements of CA1 PCs upon inactivating Som$^+$ interneurons (*25*, *26*). These effects were not observed in control mice that did not express PSAM^{L141F}-GlyR (fig. S13A). Nonspecific reduction in inhibition with $GABA_AR$ blocker bicuculine substantially increased the number of PCs responding to the air puff and their duration (fig. S13B), suggesting that other inhibitory synapses in CA1 also contribute to the control of PC population activity during aversive sensory events.

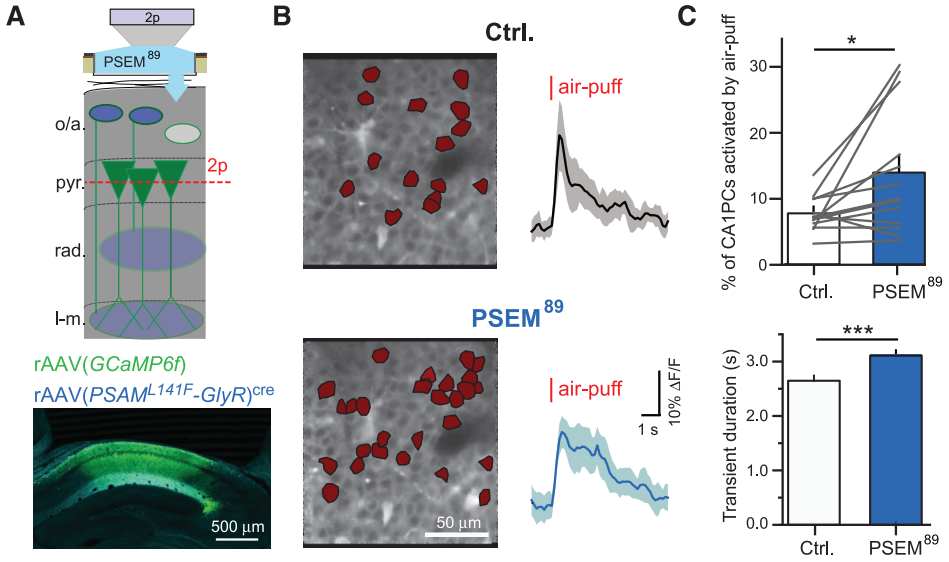

Fig. 5. Effects of inactivating CA1 Som$^+$ interneurons on US-evoked PC population activity. (**A**) (Top) Schematic of recording configuration, with 2p imaging from CA1 PC populations in the pyramidale layer of CA1 and local pharmacologenetic manipulation of PSAM^{L141F}-GlyR–expressing Som$^+$ interneurons through an aperture in the imaging window. (Bottom) Confocal image of coronal CA1 sections, with GCaMP6f expression in all neurons (green) and PSAM^{L141F}-GlyR expression in Som$^+$ interneurons, revealed by α-BTX immunostaining (blue). (**B**) (Left) Corrected time-average images of example recordings in pyr. of a mouse expressing PSAM^{L141F}-GlyR in Som$^+$ interneurons. PCs with significant US responses are marked in red. (Right) Mean $\Delta F/F$ responses of cells active in both control and PSEM^{89} conditions from left (shading is SD). (**C**) Summary data for multiple FOVs between drug conditions. (Top) Mean percentage of significantly active CA1 PCs (ctrl, 7.6 ± 0.7%; PSEM^{89}, 13.7 ± 2.5%; n = 13 FOVs; paired t test). (Bottom) Mean duration of significant transients in cells active in both drug conditions (ctrl, 2.64 ± 0.09 s; PSEM^{89}, 3.09 ± 0.09 s; n = 96 cells; paired t test). Error bars, mean ± SEM. *P < 0.05; ***P < 0.001.

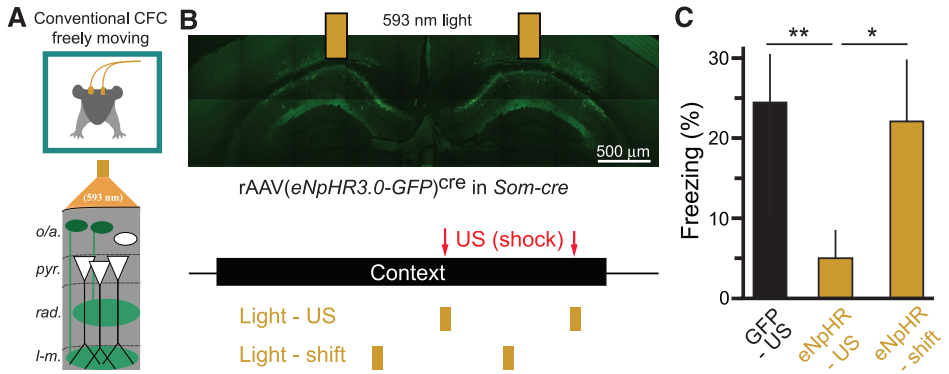

Fig. 6. Inactivating CA1 Som$^+$ interneurons during the US alone is sufficient to prevent CFC. (**A**) Schematic of optogenetic experiments in freely moving mice. Bilateral optic fibers deliver 593-nm light to inhibit eNpHR3.0-eGFP–expressing Som$^+$ interneurons in CA1 during CFC in freely moving mice. (**B**) (Top) Confocal image of eNpHR3.0-eGFP–expressing Som$^+$ interneurons in dorsal CA1 and indication of optic fiber positions. (Bottom) Experimental protocol. Mice are exposed to a context for 3 min, with two footshocks (2 s, 1 mA) 118 s and 178 s into the context. Two pulses of 593-nm light (6 s) were delivered through bilateral optical fibers starting at 116 s and 176 s (Light-US group) or 86 s and 146 s (Light-shift group). (**C**) Summary data for optogenetic stimulation experiments. GFP-US, n = 6 mice; eNpHR-US, n = 8 mice; eNpHR-shift, n = 6 mice; one-way ANOVA, $F_{(2,19)} = 3.87$, $P < 0.05$; comparisons are unpaired t tests. Error bars, mean ± SEM. *P < 0.05; **P < 0.01.

Our imaging data suggest that Som$^+$ interneurons are required for CFC because of their activation during the US. To test this hypothesis directly in a conventional CFC task, we used optogenetic methods in freely moving mice to inactivate Som$^+$ interneurons selectively during the footshock US (Fig. 6A). We expressed the light-gated Cl^- pump halorhodopsin (*56*) in Som$^+$ interneurons by injecting rAAV(*Synapsin-eNpHR3.0-eGFP*)^{cre} bilaterally into dorsal CA1 of *Som-cre* mice (fig. S14A) and implanting optic fibers over the injection sites. We used a CFC paradigm with two footshocks, which were each accompanied by coincident illumination of dorsal CA1 with 593-nm light (Fig. 6B), which suppressed spiking of Som$^+$/eNpHR3.0$^+$ neurons (fig. S14b). Inactivating Som$^+$ interneurons during the US significantly reduced conditioned freezing 24 hours later compared with controls injected with rAAV(*Synapsin-eGFP*)^{cre} (Fig. 6, B and C). Importantly, shifting the optical suppression of Som$^+$ interneurons

to 30 s before each US did not reduce freezing (Fig. 6, B and C).

Discussion

Classical fear conditioning implies a separation of CS and US prior to their association in the amygdala (*3*–*5*). In the case of cued fear conditioning (e.g., tone and shock), the brain achieves CS-US segregation by separate anatomical pathways for auditory and aversive somatosensory inputs (*57*, *58*). Standard models of CFC also assume that the hippocampus does not receive information about the US; rather, the hippocampus encodes the CS alone, whose outputs to the amygdala can be paired with the US for associative conditioning (fig. S15, A and B). However, here we observe a direct cortical excitatory input to CA1 during the US via the entorhinal cortex, indicating an anatomical overlap between sensory information for CS and US before the amygdala (*59*, *60*). This US may impede contextual conditioning (*11*). We suggest an alternative conceptual model for CFC that addresses the problem of sensory convergence in the hippocampus. In this model, subcortical neuromodulatory input drives CA1 Som^+ interneurons to selectively inhibit integration of the excitatory input pathway carrying US information to CA1. These data suggest a circuit mechanism for previously reported suppression of CA1 activity upon aversive stimulation (*37*–*40*). Compartmentalized inhibition suppresses integration of excitatory input in PC distal dendrites, which reduces US-evoked CA1 PC activity and can help limit interference of the US with CS encoding. This circuit can ensure that hippocampal output reliably encodes the CS during learning, so that memories stored downstream in the amygdala can be reactivated by exposure to the CS alone (fig. S15, C and D).

Inactivating Som^+ interneurons both increases CA1 PC activity and prevents learning. Impairments in memory storage could therefore result from a disruption of the hippocampal ensemble identity or population sparsity. The downstream mechanisms by which associative fear memories are impaired by CA1 Som^+ interneuron inactivation can be addressed by studying CS-US convergence and plasticity in the amygdala. Som^+ interneurons may also influence processing in the entorhinal cortex and medial septum through long-range inhibition (*61*). Furthermore, it remains to be determined whether US-driven excitation to CA1 contributes to long-term changes in CA1 PC activity after fear conditioning, such as place-cell remapping (*62*).

Our data suggest that inhibitory circuits can inhibit selected dendritic compartments to favor integration of one excitatory input pathway (proximal) over another (distal). GABA release localized to lacunosum-moleculare could accomplish this input segregation by inhibiting localized dendritic electrogenesis, which is required for propagating entorhinal excitatory inputs to drive output spikes and for inducing plasticity (*16*–*18*). This mechanism may also be present in sensory neocortex, where aversive footshocks activate cholinergic input to drive layer 1 interneurons in primary auditory and visual cortex (*46*). Layer 1 interneurons inhibit the apical tuft dendrites of layer 5 PCs, the primary output cell of the neocortex, at the site of multimodal association in layer 1 (*55*). Therefore the same mechanism we describe in CA1 could protect layer 5 PCs in primary sensory cortex from interference by the US, so that their outputs to the amygdala are driven by inputs to their basal dendrites reflecting local sensory processing, rather than inputs to tuft dendrites reflecting cross-modal influences.

These results suggest that dendrite-targeting Som^+ interneurons provide US-evoked inhibition that is required for successful contextual fear learning. These interneurons are central to a mechanism by which the hippocampus processes contextual sensory inputs as a CS while excluding the sensory features of the US. Selective inhibitory control over integration of excitatory input pathways could be a general strategy for nervous systems to achieve separate processing channels in anatomically overlapping circuits, a process that could be flexibly controlled by a multitude of inhibitory interneuron types (*22*, *23*) and neuromodulatory systems (*63*).

References and Notes

1. M. S. Fanselow, *Learn. Motiv.* **17**, 16–39 (1986).
2. M. S. Fanselow, *Anim. Learn. Behav.* **18**, 264–270 (1990).
3. S. Maren, *Annu. Rev. Neurosci.* **24**, 897–931 (2001).
4. J. W. Rudy, N. C. Huff, P. Matus-Amat, *Neurosci. Biobehav. Rev.* **28**, 675–685 (2004).
5. M. S. Fanselow, A. M. Poulos, *Annu. Rev. Psychol.* **56**, 207–234 (2005).
6. J. J. Kim, M. S. Fanselow, *Science* **256**, 675–677 (1992).
7. R. G. Phillips, J. E. LeDoux, *Behav. Neurosci.* **106**, 274–285 (1992).
8. S. L. Young, D. L. Bohenek, M. S. Fanselow, *Behav. Neurosci.* **108**, 19–29 (1994).
9. S. Maren, M. S. Fanselow, *J. Neurosci.* **15**, 7548–7564 (1995).
10. P. W. Frankland *et al.*, *Hippocampus* **14**, 557–569 (2004).
11. M. S. Fanselow, J. P. DeCola, S. L. Young, *J. Exp. Psychol. Anim. Behav. Process.* **19**, 121–137 (1993).
12. P. Sah, E. S. Faber, M. Lopez De Armentia, J. Power, *Physiol. Rev.* **83**, 803–834 (2003).
13. O. J. Ahmed, M. R. Mehta, *Trends Neurosci.* **32**, 329–338 (2009).
14. R. P. Kesner, *Learn. Mem.* **14**, 771–781 (2007).
15. S. Maren, M. S. Fanselow, *Neurobiol. Learn. Mem.* **67**, 142–149 (1997).
16. N. L. Golding, N. P. Staff, N. Spruston, *Nature* **418**, 326–331 (2002).
17. J. T. Dudman, D. Tsay, S. A. Siegelbaum, *Neuron* **56**, 866–879 (2007).
18. H. Takahashi, J. C. Magee, *Neuron* **62**, 102–111 (2009).
19. M. W. Jones, M. A. Wilson, *PLOS Biol.* **3**, e402 (2005).
20. K. D. Harris, H. Hirase, X. Leinekugel, D. A. Henze G. Buzsáki, *Neuron* **32**, 141–149 (2001).
21. W. Xu *et al.*, *Neuron* **73**, 990–1001 (2012).
22. T. F. Freund, G. Buzsáki, *Hippocampus* **6**, 347–470 (1996).
23. T. Klausberger, P. Somogyi, *Science* **321**, 53–57 (2008).
24. A. Losonczy, B. V. Zemelman, A. Vaziri, J. C. Magee, *Nat. Neurosci.* **13**, 967–972 (2010).
25. M. Lovett-Barron *et al.*, *Nat. Neurosci.* **15**, 423–430, S1–S3 (2012).
26. S. Royer *et al.*, *Nat. Neurosci.* **15**, 769–775 (2012).
27. W. J. Mahoney, J. J. B. Ayres, *Anim. Learn. Behav.* **4**, 357–362 (1976).
28. M. E. Bouton, R. C. Bolles, *Anim. Learn. Behav.* **8**, 429–434 (1980).
29. P. Kaifosh, M. Lovett-Barron, G. F. Turi, T. R. Reardon, A. Losonczy, *Nat. Neurosci.* **16**, 1182–1184 (2013).
30. C. J. Magnus *et al.*, *Science* **333**, 1292–1296 (2011).
31. S. G. Anagnostaras, G. D. Gale, M. S. Fanselow, *Hippocampus* **11**, 8–17 (2001).
32. I. Goshen *et al.*, *Cell* **147**, 678–689 (2011).
33. A. J. Murray *et al.*, *Nat. Neurosci.* **14**, 297–299 (2011).
34. J. Akerboom *et al.*, *J. Neurosci.* **32**, 13819–13840 (2012).
35. D. A. Dombeck, C. D. Harvey, L. Tian, L. L. Looger, D. W. Tank, *Nat. Neurosci.* **13**, 1433–1440 (2010).
36. D. A. Dombeck, A. N. Khabbaz, F. Collman, T. L. Adelman, D. W. Tank, *Neuron* **56**, 43–57 (2007).
37. O. Herreras, J. M. Solís, M. D. Muñoz, R. Martín del Río, J. Lerma, *Brain Res.* **461**, 290–302 (1988).
38. S. Khanna, *Neuroscience* **77**, 713–721 (1997).
39. M. Funahashi, Y. F. He, T. Sugimoto, R. Matsuo, *Brain Res.* **827**, 215–220 (1999).
40. O. S. Vinogradova, *Hippocampus* **11**, 578–598 (2001).
41. J. J. Lawrence, J. M. Statland, Z. M. Grinspan, C. J. McBain, *J. Physiol.* **570**, 595–610 (2006).
42. R. N. Leão *et al.*, *Nat. Neurosci.* **15**, 1524–1530 (2012).
43. S. W. Miller, P. M. Groves, *Physiol. Behav.* **18**, 141–146 (1977).
44. O. Herreras, J. M. Solís, A. S. Herranz, R. M. del Río, J. Lerma, *Brain Res.* **461**, 303–313 (1988).
45. F. Zheng, S. Khanna, *Neuroscience* **103**, 985–998 (2001).
46. J. J. Letzkus *et al.*, *Nature* **480**, 331–335 (2011).
47. H. Widmer, L. Ferrigan, C. H. Davies, S. R. Cobb, *Hippocampus* **16**, 617–628 (2006).
48. G. D. Gale, S. G. Anagnostaras, M. S. Fanselow, *Hippocampus* **11**, 371–376 (2001).
49. S. Dasari, A. T. Gulledge, *J. Neurophysiol.* **105**, 779–792 (2011).
50. M. E. Hasselmo, *Curr. Opin. Neurobiol.* **16**, 710–715 (2006).
51. L. Calandreau, R. Jaffard, A. Desmedt, *Learn. Mem.* **14**, 422–429 (2007).
52. T.-W. Chen *et al.*, *Nature* **499**, 295–300 (2013).
53. E. L. Hargreaves, G. Rao, I. Lee, J. J. Knierim, *Science* **308**, 1792–1794 (2005).
54. S. J. Zhang *et al.*, *Science* **340**, 1232627 (2013).
55. L. Palmer, M. Murayama, M. Larkum, *Frontiers in Neural Circuits* **6**, 26 (2012).
56. F. Zhang *et al.*, *Nature* **446**, 633–639 (2007).
57. L. M. Romanski, J. E. LeDoux, *Cereb. Cortex* **3**, 515–532 (1993).
58. E. Lanuza, K. Nader, J. E. Ledoux, *Neuroscience* **125**, 305–315 (2004).
59. J. Brankačk, G. Buzsáki, *Brain Res.* **378**, 303–314 (1986).
60. R. D. Burwell, D. G. Amaral, *J. Comp. Neurol.* **398**, 179–205 (1998).
61. S. Melzer *et al.*, *Science* **335**, 1506–1510 (2012).
62. M. A. Moita, S. Rosis, Y. Zhou, J. E. LeDoux, H. T. Blair, *J. Neurosci.* **24**, 7015–7023 (2004).
63. C. I. Bargmann, *Bioessays* **34**, 458–465 (2012) Supplementary References.

Acknowledgments: We thank S. Sternson and P. Lee for proving PSEM[89], A. Castro for programming assistance, E. Balough and M. Cloidt for scoring freezing, R. Field for preparing brain slices, J. Tsai for assistance with histology, T. Machado for assistance with *ChAT-cre* mice, W. Fischler for assistance with odor stimuli, and C. Lacefield for assistance with behavioral apparatus. M.L.-B. was supported by an Canadian Natural Sciences and Engineering Research Council postgraduate scholarship. P.K. is an Howard Hughes Medical Institute International Predoctoral Fellow. M.A.K. is supported by NIMH K01MH099371, the Sackler Institute, and a NARSAD Young Investigator Award. R.H. is supported by NIH R37 MH068542, NIA R01 AG043688, New York State Stem Cell Science, and the Hope for Depression Research Foundation. B.V.Z. is supported by the Human Frontier Science Program. A.L. is supported by the Searle Scholars Program, the Human Frontier Science Program, and the McKnight Memory and Cognitive Disorders Award.

Supplementary Materials

www.sciencemag.org/content/343/6173/857/suppl/DC1
Materials and Methods
Figs. S1 to S15
References (*64*–*66*)

22 October 2013; accepted 23 January 2014
10.1126/science.1247485

Dendritic Inhibition in the Hippocampus Supports Fear Learning

Matthew Lovett-Barron, Patrick Kaifosh, Mazen A. Kheirbek, Nathan Danielson, Jeffrey D. Zaremba, Thomas R. Reardon, Gergely F. Turi, René Hen, Boris V. Zemelman and Attila Losonczy

(February 20, 2014)
Science **343** (6173), 857-863. [doi: 10.1126/science.1247485]

Editor's Summary

Fear, Memory, and Place

Contextual fear conditioning (CFC) is widely used as a hippocampal-dependent classical conditioning task to model human episodic memory. **Lovett-Barron *et al.*** (p. 857) combined in vivo imaging with pharmacology, pharmacogenetics, and optogenetics and they found that somatostatin-expressing, dendrite-targeting γ-aminobutyric acid–releasing interneurons in hippocampal area CA1 are required for CFC. During CFC, sensory features of the aversive event reach hippocampal output neurons through excitatory cortical afferents and require active inhibitory filtering to ensure that the hippocampus exclusively encodes the conditioned stimulus.

Science (print ISSN 0036-8075; online ISSN 1095-9203) is published weekly, except the last week in December, by the American Association for the Advancement of Science, 1200 New York Avenue NW, Washington, DC 20005.

www.sciencemag.org/cgi/content/full/343/6173/857/DC1

Supplementary Materials for

Dendritic Inhibition in the Hippocampus Supports Fear Learning

Matthew Lovett-Barron, Patrick Kaifosh, Mazen A. Kheirbek, Nathan Danielson, Jeffrey D. Zaremba, Thomas R. Reardon, Gergely F. Turi, René Hen, Boris V. Zemelman, Attila Losonczy*

*Corresponding author. E-mail: al2856@columbia.edu

Published 21 February 2014, *Science* **343**, 857 (2014)
DOI: 10.1126/science.1247485

This PDF file includes:

Materials and Methods
Figs. S1 to S15
References

Materials and Methods

All experiments were conducted in accordance with the US National Institutes of Health guidelines and with the approval of the Columbia University and New York State Psychiatry Institute Institutional Animal Care and Use Committees.

Mice and Viruses

In all experiments we used adult mice of either sex, that were either wild-type C57/Bl6 mice, ChAT-cre mice (Jackson, #006410), or the hemizygous offspring of Som-Cre or Pvalb-cre mice with the Ai9 reporter line (loxP-STOP-loxP-tdTomato Cre reporter strain B6;129S6-Gt(ROSA)26Sortm9(CAG-tdTomato)Hze/J (Jackson Laboratory)) on a C57/Bl6 background, have previously reported (*25*).

We used the following viruses: rAAV2/1(*synapsin-PSAM*$^{L\text{-}141F}$*-GlyR*), rAAV2/7(*Synapsin-PSAM*$^{L\text{-}141F}$*-GlyR*)^{cre} (*25,30*), rAAV2/1(*Synapsin-GCaMP5G*) (*29,34*), rAAV2/7(*Synapsin-GCaMP5G*)^{cre}, rAAV2/1(*Synapsin-GCaMP6f*), rAAV2/7(*Synapsin-GCaMP6f*)^{cre} (*52*; Penn vector core), rAAV2/7(*Synapsin-eNpHR3.0-eGFP*)^{cre}, rAAV2/7(*Synapsin-tdTomato*)^{cre}, or rAAV2/7(*Synapsin-eGFP*)^{cre}. For targeting ChAT+ neurons in the medial septum, rAAV2/1(*ef1α-DIO-GCaMP6f*)^{cre} was created by cloning the GCaMP6f gene (Addgene 40755) into the Cre-conditional vector, rAAV-*ef1α*-DIO-hChR2(H134R)-EYFP-WPRE-pA (Addgene 20298), replacing the existing hChR2-EYFP insert. Restriction sites 5' NheI and 3' AscI were used, and only the core of GCaMP6f was maintained after removing the 5' 6xHis tag. A chimeric serotype 1+2 of AAV was prepared (*64*) for stereotaxic injection. This specific serotype and viral promoter were required to gain reliable expression in ChAT-positive cells, as *synapsin* (serotypes 2/1 & 2/7) and *CAG* (serotype 5) viruses were ineffective for labeling these neurons. Stereotaxic viral injections were performed using a Nanoject syringe, as described previously *(25,29).* Recordings from eNpHR3.0-GFP/Som+ interneurons in CA1 were performed as described previously (*25*), and cells were stimulated using the same 593nm laser used for *in vivo* experiments.

Surgery

Hippocampal window

Hippocampal window implant surgeries were performed as described previously (*29,35*). Briefly, we anesthetized mice with isoflurane and treated them with buprenorphine (0.1 mg/kg, subcutaneous) to minimize post-operative discomfort. We exposed the skull and drilled a 3-mm diameter circle centered over left dorsal CA1, matching the size of the cannula window to be implanted. We removed the bone and dura, and then slowly aspirated cortex covering the hippocampus while constantly irrigating with chilled cortex buffer until the external capsule was exposed. If the alveus (anterior-posterior fibers) became exposed, surgery was terminated. Otherwise, we implanted the sterilized window implant by wedging it into place, and secured the top of the cannula to the skull and stainless steel headpost with grip cement, leaving it to dry for 15–20 min before returning mice to the home cage (awake and mobile in 5–20 min). We monitored mice every 12 hours for three days after surgery, administering buprenorphine to minimize any signs of discomfort.

Optical fibers

We used published techniques for the construction of chronically dwelling optical fibers and patch cables for optogenetic behavioral procedures (*65*). For all experiments, a 200 μm core, 0.37 numerical aperture (NA) multimode fiber was used for optical stimulation via a patch cable connected to either a 100 mw 593.5 or 473 nm laser diode. Adult mice were surgically implanted with fiber optic cannulas using published protocols (*65*).

Head-fixed stimulus presentation and behavioral readout

We developed a flexible system for combining two-photon imaging with microcontroller-driven stimulus presentation and behavioral read-out, as previously described (*29*). Briefly, tones were presented with speakers near each of the mouse's ears, light flashes lasting 200 ms were delivered with a red LED, and odor stimuli and air-puffs were delivered via separate solenoid valves to gate airflow from a compressed air tank to a tube ending in a pipette tip facing the mouse's snout. Odor was delivered with lower pressure air, and passed through a filter covered in a 50:50 mixture of odorant with mineral oil (50 μL). We tracked locomotion by measuring treadmill wheel rotation,

recorded as changes in voltage across an infrared photo-transistor as wheel spokes blocked light from an infrared LED. Electrical signals encoding mouse behavior and stimulus presentation were collected with an analog to digital converter, which was synchronized with two-photon imaging by a common trigger pulse.

We used headpost-implanted adult mice for all experiments. In the case of hf-CFC experiment, starting 3–7 days after implantation we water-restricted mice (>85% pre-deprivation weight) and habituated them to handling and head-fixation. Within 3 or 4 sessions, mice could undergo extended head-fixation while appearing calm, but alert, and periodically running while freely licking for small-volume (~0.5 μl/lick) water rewards during imaging sessions. During the hf-CFC task, mice could lick for water for 4.5 min – 1 m pre context, 3 min context, and 30 s post-context. This protocol was repeated twice a day for three days (Habituation, Conditioning, and Recall), with 1-3 hours between each context. Each context CS consisted of a distinct set of auditory, visual, olfactory, and tactile cues that we presented to mice using a microcontroller-driven stimulus presentation and behavioral recording system (**Fig. S1a**)(*29*). On the second day (Conditioning) we presented mice with both contexts again, but paired one context (CtxC) with a US: six air-puffs to the snout (200 ms, 0.1 Hz) during the final minute of the context. The other context was neutral and not paired with a US (CtxN). On the third day (Recall), we exposed mice to the conditioned context (CtxC) and the neutral context (CtxN) again, and assessed the rate of licking in each context.

For discrete stimulus presentation, we habituated mice to handling and head-fixation, but did not water-restrict them. We used a variable inter-stimulus interval of 20–40 s between stimuli, which were repeated 5–10 times for each modality in a pseudorandom order. To characterize responses to air-puffs of varying durations, we repeated stimulation with durations from 10 ms to 500 ms; each level was presented 3 times, interspersed with 200 ms tones.

Freely-moving behavior

Fear Conditioning – PSAM^{L141F}-GlyR experiments

Fear conditioning took place in fear-conditioning boxes that contained one clear plexiglass wall, three aluminum walls, and a stainless steel grid as a floor. All mice were

injected with PSEM^{89} (60 mg/kg i.p. in saline) 15 min prior to conditioning. The training session began with the onset of the houselight and fan, and anise scent was placed under the grid floor. In this one-trial contextual fear conditioning protocol, 180 s after placement of the mouse in the training context and onset of houselight and fan, mice received a single 2 s footshock of 1 mA. All freezing was measured before the single footshock. The mouse was taken out 15 s after termination of the footshock and returned to its home cage. The grid and the waste tray were cleaned with Sanicloths between runs. The recall session occurred 24 hours later in the same chamber, but without PSEM^{89} injection or footshocks. Mice were recorded by video cameras mounted above the conditioning chamber and were scored for freezing by an investigator blind to the experimental condition of the animal.

Fear Conditioning – Tone conditioning

All mice were injected with PSEM^{89} (60 mg/kg i.p. in saline) 15 min prior to conditioning. For cued fear conditioning, mice were trained in the same context as in CFC, except that a 20 s, 80 dB, 2 kHz pure tone was provided as the discrete cue CS, and a 2 s footshock that co-terminated with the tone was provided. This was repeated three times. Twenty-four hours later, mice were tested for cued fear in a novel context, in which the conditioning chamber was altered, the stainless steel grid floor was covered with a plastic panel and novel cage bedding, the chamber walls were covered and made circular using colored plastic inserts, the house fan and lights were turned off, and no scent was used. The tone was presented three times, and an investigator blind to condition scored freezing before the first tone presentation and during each tone presentation as a measure of cued fear.

Fear Conditioning – optogenetic experiments

In the case of optogenetic manipulations during conditioning, mice were quickly attached to the fiber optic patch cables (bilaterally) via a zirconia sleeve, then placed in a novel cage bottom for five minutes prior to being placed in the testing apparatus. The patch cables were interfaced to an FC/PC rotary joint, which was attached on the other end to a 593 nm laser diode that was controlled by a Master-8 stimulator, as previously described (*65*). In these experiments, mice were exposed to two 2 s shocks (1 mA) separated by one minute; shocks were paired with 6 s optogenetic stimulation (593 nm)

centered over the shock (Light-US condition) or shifted 30 s before each shock (Light-shift condition). All mice were processed for histology, and subjects were excluded from the study if the implant entered the hippocampus, if viral infection was not complete, or if the viral infection was not limited to CA1 Som+ interneurons.

Delayed non-match to sample

Mice were food-restricted for 1 day prior to experiments. Mice pursued sweetened condensed milk rewards (50% dilution, 30 µL) (*66*). Mice were injected with 60 mg/kg PSEM^{89} i.p., and tested in a delayed non-match to sample task in a y-maze from 10-35 min post-injection. Mice performed 10 trials, in which the mouse began in the start box, and consisting of a sample phase (shuffling of location across trials), a 30 s delay phase in the start box, and a sample phase, where the correct response is to go to the arm not yet visited. Between trials mice were moved to a clean cage for 60 s, and the location of the sample arm was shuffled. Animals were scored as the % correct trials, and trials were omitted if mice took >90 s on the sample phase, or >120 s on the choice phase.

2-photon imaging

We use an *in vivo* X-Y galvanometer-mounted mirror-based multi-photon microscopy system and an ultra-fast pulsed laser beam (920-nm wavelength; 20–40 mW average power at the back focal plane of the objective) controlled with an electro-optical modulator to excite GCaMP and tdTomato through a 40X objective. Distilled water or warmed cortex buffer (in the case of acute pharmacology experiments) served to connect the water immersion objective with the cannula. Green and red fluorescence were separated with an emission filter cube set (green, HQ525/70m-2p; red, HQ607/45m-2p; 575dcxr). Fluorescent light was detected with photomultiplier tubes (green GCaMP fluorescence, GaAsP PMT; red tdTomato fluorescence, multi-alkali PMT) operated with PrairieView software. Once mice were head-fixed, we used goniometers (Edmund Optics) to adjust the angle of the mouse's head up to 10 degrees to make the imaging window parallel to the objective. Time series were collected in red (tdTomato signal) and green (GCaMP signal) channels at 256 × 128 pixels covering 150 × 150 µm at 7.63 Hz (cell bodies, interneuron axons), or 256 × 256 pixels covering 75 × 75 µm at 4.02 Hz (CA3, LEC, and ChAT+ axons). Time-series were motion-corrected as

described in ref. *29*, adapted from methods established in ref. *36*. Regions of interest (ROIs) were manually drawn over corrected time-series in Image J (NIH), to isolate the somas or axons of cells of interest. Trials with running were excluded from summary analyses of sensory responses in interneurons and excitatory axons.

Local pharmacology during 2-photon imaging

For local pharmacology experiments, we replaced the glass coverslip with a plastic coverslip with a punctured hole (~200 μm diameter) (*29*). This hole was plugged by a plastic bar and Kwik-Sil. Instead of waiting several days to perform experiments, mice were habituated and tested 1–5 days after implants. Before imaging, we removed the plastic plug and filled the cannula with warmed (~32 °C) cortex buffer (125 mM NaCl, 5 mM KCl, 10 mM glucose, 10 mM HEPES, 2 mM $CaCl_2$ and 2 mM $MgCl_2$). After control imaging, we filled the cannula and fluid well for the objective with cortex buffer containing dissolved scopolamine (1 mM), pirenzepine (0.01-1 mM), mecamylamine (1 mM), NBQX (20 μM), PSEM^{89} (500 μM), or bicuculine (20 μM) and allowed 30-90 min for drug diffusion before imaging.

Identification of significantly responding PCs

Approximately 150-200 ROIs were drawn over putative PCs for each field of view. Statistically significant calcium transients were identified automatically using an approach similar to that described by ref. *36*. Briefly, negative deflections in the $\Delta F/F$ trace are assumed to be due to motion out of the z-plane. Because cells should move into the imaging plane with the same frequency they leave this plane, positive and negative deflections in the $\Delta F/F$ curve that are attributable to motion should occur at the same frequency. Therefore we calculate a false positive event detection rate by dividing the number of negative deflections for a given amplitude and duration by the number of positive deflections at the same magnitude and duration. As signal-to-noise ratio can vary on a per-cell basis, event amplitudes are calculated in terms of the standard-deviation (σ) of the $\Delta F/F$ trace, which provides an estimate of noise for the cell. Transient onsets are defined as the times when the $\Delta F/F$ exceeds 2 σ, and offset is defined as the time at which $\Delta F/F$ falls below 0.5 σ. A decaying exponential was fit by

least-squares to the false positive rate values, allowing for the determination of a minimum transient duration at each σ level at different confidence levels (**Fig. S12**).

We analyzed sensory responses in PCs using peri-stimulus-time-histograms (PSTHs). To calculate PSTHs, a binary activity function of time was computed for each cell, indicating whether it was in a significant calcium transient (95% confidence). Time series were aligned by stimulus time, and the binary-activity functions across stimulus presentations were averaged at each time point in a window +/- 20 frames from the stimulus, yielding a PSTH of the binary activity function for each cell and stimulus. The response-value was defined as the mean of the 20 post frames minus the mean of the 20 pre frames. To assess confidence, alignment times were shuffled 10000 times, yielding a distribution of response-values. A cell was deemed significantly responsive if the true response-value exceeded the 95th percentile of the shuffle distribution. For significantly-responsive cells, PSTHs of the ΔF/F traces were computed similarly. For the analysis of PSEM and bicuculine effects on PC population (**Fig. 5** and **Fig. S13**), fields of view containing fewer than 3% responsive cells were omitted.

Immunohistochemistry & confocal imaging

After imaging experiments, virally-injected mice were deeply anesthetized with isoflurane and perfused with 4% paraformaldehyde dissolved in 0.1 M phosphate-buffered saline (pH = 7.4). Brains were removed, sectioned at 50-60 µm and either mounted for confocal microscopy or processed for immunofluorescence staining. In mice expressing PSAM^{L141F}-GlyR, we performed immunostaining of the hybrid PSAM^{L141F}-GlyR channel as detailed previously (*25,29,30*), using Alexa 647–conjugated α-bungarotoxin (α-BTX, 1:3000), selective for the mutated α7-nAChR receptor binding site of PSAM^{L141F}-GlyR. Confocal stack images (40–50 slices, 1-2 µm optical thickness) were collected from dorsal CA1 region with a 20X objective. Stacks were collapsed into one z-plane, and cell bodies that were labeled for tdTomato and/or α-BTX Alexa 647 were counted in the *oriens/alveus* and/or *pyramidale* layers of CA1 (ImageJ, US National Institutes of Health), allowing for quantification of the density and overlap of neuronal expression. In mice expressing GCaMP6f in ChAT+ cells of the medial septum, slices were immunostained with ChAT antibodies (AB144P; Millipore; 1:500

dilution) and detected with 1:500 concentration of anti-goat DyLight 649 (Jackson ImmunoResearch). Confocal tile-stack images (2,535 slices, 1 μm optical thickness) from the medial septum were acquired using a (20X objective), and counted for GCaMP6f and ChAT co-localization as described above.

Data analysis

hf-CFC was scored by automated measurement of the rate of licks in each context (capacitive transients measured from metal water port), as described previously (*29*). Freely-moving conditioning was assessed by freezing scored by a trained observer blind to the experimental condition. Head-fixed contextual fear conditioning behavioral data, delayed non-match to sample behavioral data, and responses by stimulus and cell type were analyzed with two-way ANOVA, with repeated measures in cases that the same subject was used across multiple conditions. Pair-wise comparisons were performed with sign tests for paired data and Mann-Whitney U tests for unpaired data. Sign tests were used to assess pharmacological effects on calcium responses, and Mann-Whitney U tests were used to assess pharmacogenetic effects on head-fixed contextual fear conditioning and differences in running-related activity across cell types. PC population imaging data was analyzed with paired or unpaired t-tests in the cases of % active cells and transient durations, respectively. Statistical tests on imaging data were performed treating each field-of-view as an independent observation by averaging the responses from all simultaneously imaged ROIs. Statistical comparisons were 1-way or 2-way ANOVAs, with pairwise sign tests or unpaired Mann-Whitney U tests, or paired and unpaired t-tests. All tests were two-sided, and the type of statistical test is noted in each case. All summary data are presented as mean ± s.e.m. *p <0.05, **p <0.01, ***p <0.001.

Supplementary References

64) McClure, C., Cole, K.L., Wulff, P., Klugmann, M., and Murray, A.J. (2011). Production and titering of recombinant adeno-associated viral vectors. *J Vis Exp*, **57**, e3348, doi:10.3791/3348.

65) Kheirbek, M.A., *et al.* (2013). Differential control of learning and anxiety along the dorsoventral axis of the dentate gyrus. *Neuron,* **77**, 955-968.

66) Deacon, R.M.J., and Rawlins, J.N.P. (2006). T-maze alternation in the rodent. *Nature Protocols*, **1**, 7-12.

Supplementary Figures

Fig. S1. Details of hf-CFC task and controls

a) Details about the two contexts used in the hf-CFC task. **b**)-**e**) Control experiments for the hf-CFC task – of mice that received no experimental manipulation, some received surgical or behavioral treatments whereas others did not. None of these treatments altered hf-CFC performance. **b**) Implant and imaging control: 'Imaging' group (n = 9) – mice express GCaMP, have a hippocampal window implanted, and have CA1 imaged with a 2-photon microscope during hf-CFC. 'No imaging' group (n = 12) – mice are implanted with a headpost alone with no window surgery or imaging. Unpaired t-test: p = 0.705. **c**) Viral expression control: 'Virus' group (n = 11) – mice have received stereotaxic injections of a virus to express tdTomato, GFP, or GCaMP. 'No virus' group (n = 10) – mice received no viral injection. Unpaired t-test: p = 0.828. **d**) PSEM injection control: 'PSEM' group (n=11) – mice were injected with 60 mg/kg PSEM^{89} in saline i.p 15 min before conditioning in CtxC session. These mice were used as the control group in Figure 1e. 'No PSEM' group (n=10) – mice received no PSEM^{89} injection. Unpaired t-test: p = 0.252. **e**) Context identity control: 'CtxC = 1' group (n = 10) – mice were conditioned to Context 1 (CtxC), and Context 2 was neutral (CtxN). 'CtxC = 2' group (n = 11) – mice were conditioned to Context 2 (CtxC), and Context 1 was neutral (CtxN). Unpaired t-test: p = 0.652. f) Mean lick rates for each group in Fig.1e, displaying the mean total lick rate across all sessions (baseline for learning index), and the mean lick rate in recall of CtxC and CtxN.

Fig. S2. Viral expression of PSAM^{L141F}-GlyR in CA1 Som+ or Pvalb+ interneurons of dorsal CA1

a) Septo-temporal extent of viral expression of the ligand-gated Cl- channel PSAM^{L141F}-GlyR in dorsal CA1, revealed by α-bungarotoxin/Alexa647 (*α-BTX IHC*) immunostaining (example *Som-cre* and *Pvalb-cre* mice). **b**) Mean % of cre/tdTomato+ cells in CA1 that are also PSAM^{L141F}-GlyR+ in *Som-cre/Ai9* (5 sections) and in *Pvalb-cre/Ai9* (6 sections) mice. **c**) Counts in *Som-cre/Ai9* mice from panel b) were restricted to *oriens*, because a sparse subset of CA1 PCs in *pyramidale* express tdTomato developmentally, but do not express cre in adulthood.

Fig. S3. PSAM^{L141F}-GlyR inactivation of CA1 interneurons during freely-moving CFC and tone conditioning

a) Schematic of experimental protocol. Mice were injected with 30 mg/kg PSEM^{89} i.p. 15 min before CFC with a single 2 s/1 mA footshock, and are tested in a recall session 24 hours later without PSEM^{89}. **b**) Summary data for contextual freezing 24 hours later with *Som-cre* mice and *Pvalb-cre* mice, expressing either tdTomato or PSAM^{L141F}-GlyR in cre+ CA1 interneurons (2-way ANOVA, genotype x virus: $F_{(1,31)} = 5.43$, $p < 0.05$). *Som-cre* mice, control vs. PSAM^{L141F}-GlyR ($p < 0.05$); *Pvalb-cre* mice, control vs. PSAM^{L141F}-GlyR ($p = 0.75$), unpaired 2-tailed t-test. **c**) Summary data for tone-conditioning experiments with *Som-cre* and *Pvalb-cre* mice. Mice were injected with 60 mg/kg PSEM^{89} i.p. 15 min before conditioning with four 20 s tones terminating with a 2 s/1 mA footshock. Freezing was assessed 24 hours later in an altered context without PSEM^{89}, tested with four repetitions of 20 s tones. *Som-cre*: control, n=2; PSAM^{L141F}-

GlyR, n=2; p = 0.56, unpaired 2-tailed t-test. *Pvalb-cre*: control, n=4; PSAM^{L141F}-GlyR, n=4; p = 0.839, unpaired 2-tailed t-test.

Fig. S4. Effects of inactivating CA1 Som+ interneurons on learning is not a consequence of brain-state effects
Som-cre mice were injected with 60 mg/kg PSEM^{89} in saline i.p. 15 min before CtxC conditioning session, and CtxC recall session. Unpaired 2-tailed t-test: $p < 0.01$. Because these mice were similar to *Som-cre* mice injected with PSEM^{89} during conditioning alone, the two groups were merged for Fig. 1e.

Fig. S5. Inactivating CA1 Pvalb+ interneurons with PSAM^{L141F}-GlyR disrupts spatial working memory
a) Schematic of experimental protocol. Mice pursued sweetened condensed milk rewards (50% dilution, 30 µL). Mice were injected with 60 mg/kg PSEM^{89} i.p., and tested in a delayed non-match to sample task in a y-maze from 10-35 min post-injection. Mice went through 10 trials beginning in the start box, consisting of a sample phase (shuffling of location across trials), a 30 s delay phase in the start box, and a choice phase. The correct response in the choice phase is to collect a reward in the arm not yet visted, reflecting working memory in a natural foraging behavior. Between trials mice were moved to a clean cage for 60 s. **b**) Summary data for DNMS task, in *Som-cre* and *Pvalb-cre* mice (2-way ANOVA, genotype x virus: $F_{(1,23)} = 2.0$, $p = 0.172$). There was a significant main effect of virus ($p < 0.005$). *Som-cre* mice, Control vs. PSAM^{L141F}-GlyR ($p = 0.173$); *Pvalb-cre* mice, control vs. PSAM^{L141F}-GlyR ($p < 0.05$), Mann-Whitney U tests.

Fig. S6. Fraction of sensory-evoked responses by cell types in CA1
a) Expression of GCaMP5G in CA1 *oriens* interneurons of a *Som-cre/Ai9* mouse, including parallel recording from Som/tdTom+ and Som/tdTom- interneurons. **b**) Left: traces from example cells in panel *a* during the pseudorandom presentation of discrete sensory stimuli. Traces are concatenated together from 30 individual trials of air-puffs, tones, and lights. Middle: example averaged air-puff responses on an expanded time scale. Right: The same data represented as heat maps, with trials grouped by stimulus type. **c**) Summary data for GCaMP5G responses to discrete sensory stimuli in Som+ and Som- interneurons (*Som-cre/Ai9* mice), Pvalb+ interneurons (*Pvalb-cre/Ai9*), and pyramidal cells (both lines). $\Delta F/F$ is calculated using the difference between the 5 s before and after stimulus onset.

Fig. S7. Local pharmacological manipulation of imaged tissue
a) Spread of 1% Evans Blue (in cortex buffer) through the perforated imaging window over the timescale of pharmacological manipulation, followed by perfusion, fixation, and mounting. **b**) Concentration-dependence of m1AChR blockade on air-puff-evoked activity in Som+ interneurons. Each line is one Som+ cell (n=13 cells). **c**) Responses of pyramidal cells to air-puffs (see Supplementary Figure 12 & 13) are not significantly altered by the concentration of pirenzepine (100µM) required to block Som+ interneuron responses to air-puffs. We measured this as the duration of air-puff-evoked transients in

PCs active in both drug conditions (ctrl: 2.51 ± 0.3s, Pir.: 2.84 ± 0.5s, n = 5 cells; paired t-test), as in Fig. 5 and Fig. S13.

Fig. S8. Expression of GCaMP6f in ChAT+ neurons of the medial septum and imaging their axons in CA1

a) Top: Confocal images of the medial septum showing co-localization of virally expressed GCaMP6f and endogenous ChAT with ChAT immunohistochemistry. Bottom: Summary graph of co-localization of ChAT immunohistochemistry and GCaMP labeling (n = 3 section in 3 mice) in ChAT-cre mice injected with rAAV2/1(*ef1α-DIO-GCaMP6f*)^{cre} into the medial septum. **b**) More examples of FOVs from *oriens/alveus* in CA1 of ChAT+ mice, and the ROIs drawn to analyze axonal signals. **c**) Responsiveness of ChAT+ axons to locomotion on the treadmill.

Fig. S9. ChAT+ and Som+ axons are sensitive to the onset of air-puffs, but not the duration

Mean responses to air-puffs of duration 10 ms, 30 ms, 50 ms, 100 ms, 150ms, 200 ms, 300 ms, and 500 ms in: **a**) ChAT+ axons (individial axon ROIs averged over FOVs, as in Figure 3d-e) in *oriens/alveus* (*o/a.*). **b**) Som+ axons (whole-field ROIs in *lacunosum-moleculare* (*l-m.*), as in Figure 2c-e).

Fig. S10. Imaging GCaMP6f-expressing excitatory projections to CA1

a) Injection sites of rAAV(*Synapsin-GCaMP6f*) into CA3 (left), LEC (middle), or MEC (right) ipsilateral to the imaged hemisphere of CA1. **b**) Locomotion signals in CA3, LEC, and MEC axons (whole-field ROIs). **c**) Example responses of single CA3 axons to running and air-puffs. While most CA3 axons do not respond to air-puffs, as reflected in whole-field fluorescence (Fig.. 4), a sparse subset of CA3 axons do respond, potentially providing the drive to excite a sparse subset of CA1 PCs, even though the much stronger LEC and MEC signals are being inhibited.

Fig. S11. PSEM^{89} inactivation of Som+ interneurons *in vivo*

Mean air-puff responses of Som+/PSAM^{L141F}-GlyR+ interneurons (left) and Som−/PSAM^{L141F}-GlyR− interneurons (right) in control and PSEM^{89} administration (60 mg/kg PSEM^{89} i.p. 12-30 min before stimulus presentation).

Fig. S12. Identification of pyramidal cells with significant stimulus-evoked activity

a) Histograms of positive (blue) and negative (red) deflections in the ΔF/F trace. Event amplitudes are quantified in terms of σ, which is determined for each cell and is defined as the standard deviation of the noise of the cell's ΔF/F trace. Histograms show the distribution of event durations for events greater than or equal to each σ level. **b**) False positive rates for 2-, 3-, and 4-σ events (pooled across all FOVs in all mice used in Fig. 5 and Fig. S13). False positive rate curves are calculated for each σ level by dividing the number of negative events at that level by the number of positive events at that level. See ref. *33* for more details. Event onsets are defined as the times when the ΔF/F exceeds 2-σ, and offset is defined as the time at which the ΔF/F falls below 0.5 σ. A decaying exponential was fit by least-squares to the false positive rate values,

allowing for the determination of a minimum transient duration at each σlevel for different confidence levels.

Fig. S13. Effects of local PSEM and bicuculine on PC populations
a) $PSEM^{89}$ does not alter the mean % of active cells during air-puffs (ctrl: 10.1 ± 2.6%, $PSEM^{89}$: 7.1 ± 1.3%, n=4 FOVs; paired t-test) or the duration of air-puff-evoked transients in cells active in both drug conditions (ctrl: 2.73 ± 0.2s, $PSEM^{89}$: 2.56 ± 0.2s, n = 21 cells; paired t-test) in mice that do not express $PSAM^{L141F}$-GlyR. **b**) 20 μM Bicuculine increases the mean % of active cells during air-puffs (ctrl: 7.6 ± 0.7%, Bic.: 41.3 ± 6.7%, n=13 FOVs; paired t-test) and the duration of air-puff-evoked transients in cells active in both drug conditions (ctrl: 2.72 ± 0.09 s, Bic: 3.21 ± 0.09 s, n = 114 cells; paired t-test). Bars represent mean ± s.e.m., ***p < 0.001, ns = non-significant

Fig. S14. Expression of eNpHR3.0-eGFP in CA1 Som+ interneurons
a) Left: example confocal image of eNpHR3.0-eGFP expression in dorsal CA1 of injected *Som-cre* mice. Right: Mean % of cre/tdTomato+ cells in *oriens* that are also eNpHR3.0-eGFP+. **b**) Top left: Example cell-attached recording from Som+/eNpHR3.0-eGFP+ neuron *ex vivo*, showing suppression of spontaneous spiking with 593 nm light. Bottom left: Example whole-cell current clamp recording from Som+/eNpHR3.0-eGFP+ neuron *ex vivo*, showing hyperpolarization with 593 nm laser light at two resting voltages. Right: example whole-cell current clamp recordings from Som+/eNpHR3.0-eGFP+ neuron *ex vivo*, with overlapping laser light and current injection.

Fig. S15. Hypothesized conceptual model of CFC
a) Schematic of sensory processing in the case of fear conditioning to a unimodal CS, such as a tone. **b**) Schematic of sensory processing in the case of fear conditioning to a multimodal contextual CS, which requires the hippocampus to form a unified respresentation of the context from disparate sensory cues. **c**) Traditional view of CFC. The hippocampus processes the context CS independent of the sensory features of the US. **d**) We propose an alternative conceptual model of CFC. Sensory information about the US can reach CA1 through direct inputs from the entorhinal cortex, requiring active filtering. The US also sends parallel signals to the medial septum cholinergic system, which excites CA1 dendrite-targeting interneurons to prevent US signals from influencing hippocampal CS processing.

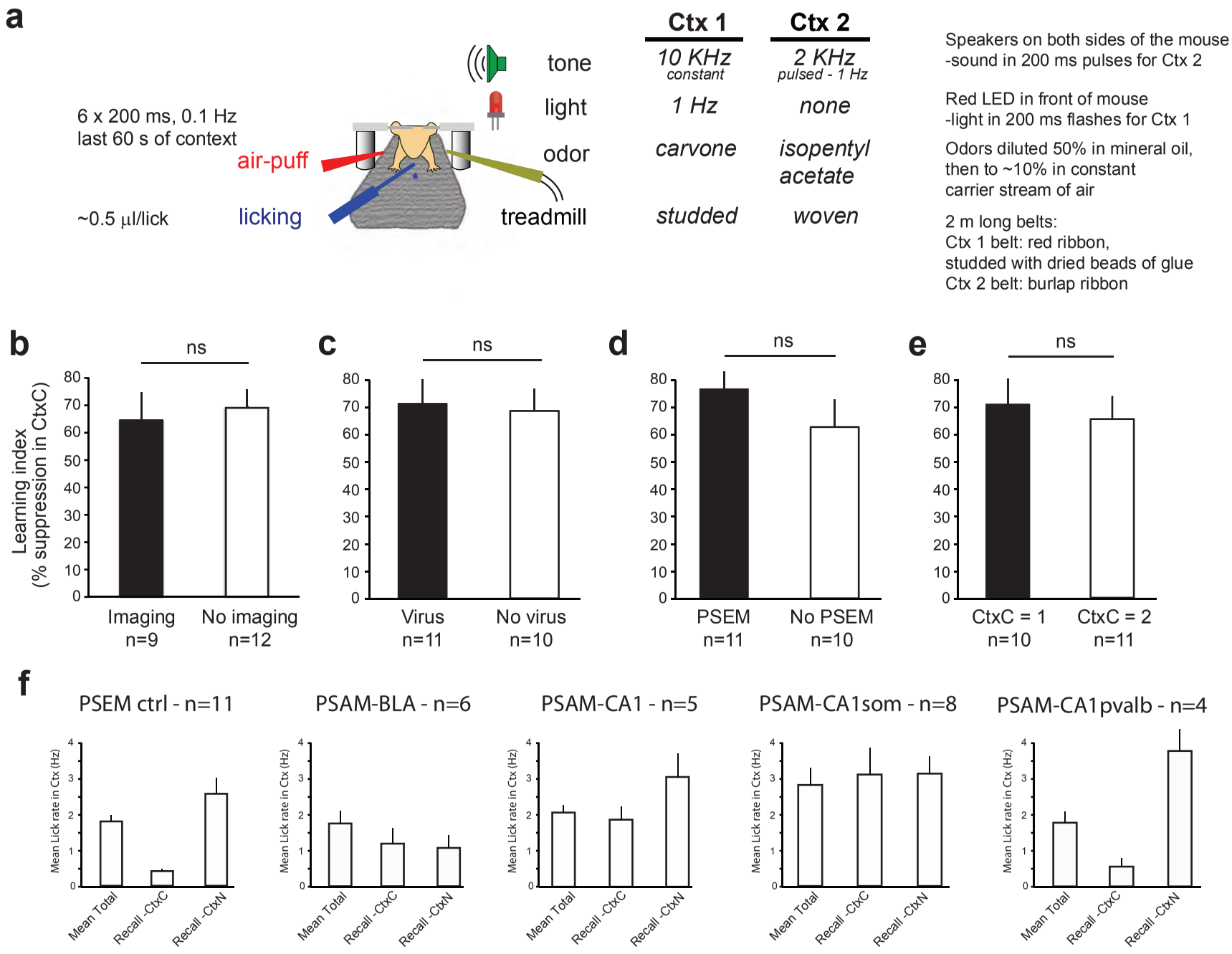

Supplementary Figure 1
Lovett-Barron et al.

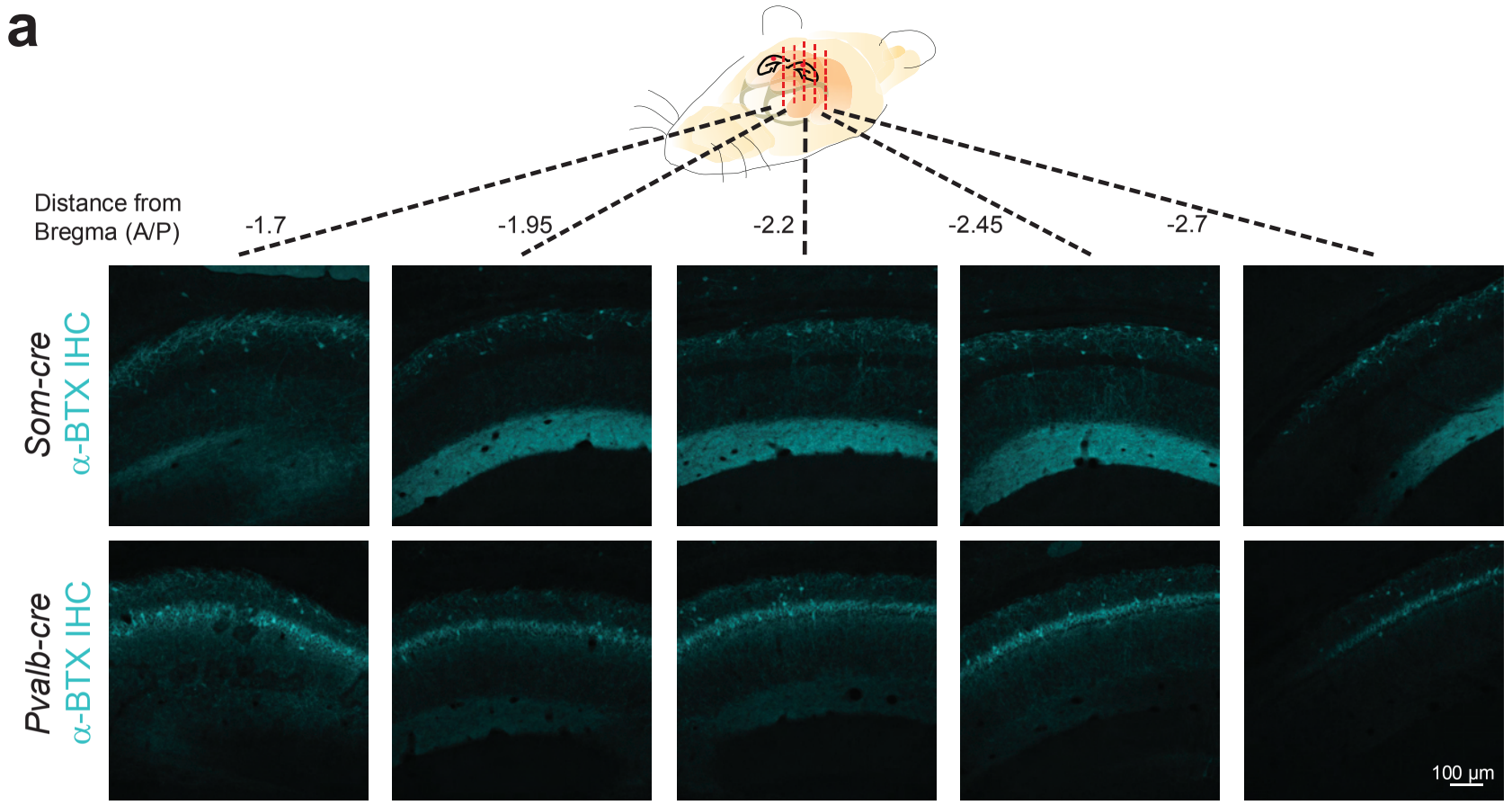

Supplementary Figure 2
Lovett-Barron et al.

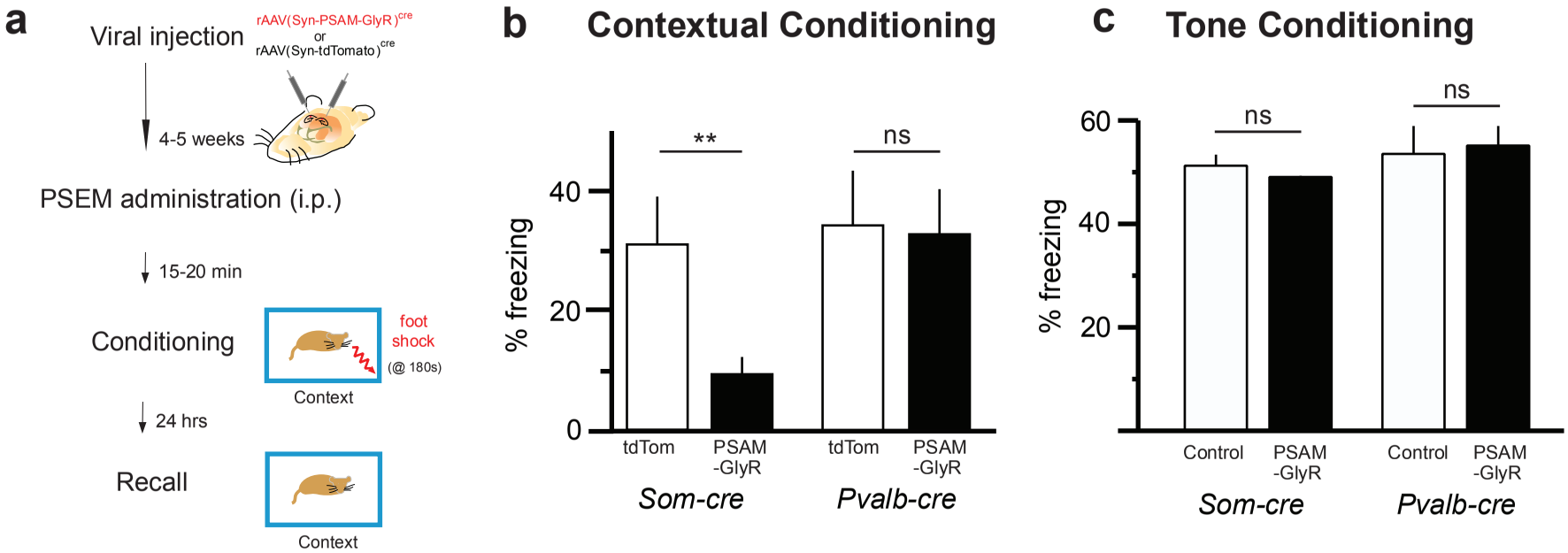

Supplementary Figure 3
Lovett-Barron et al.

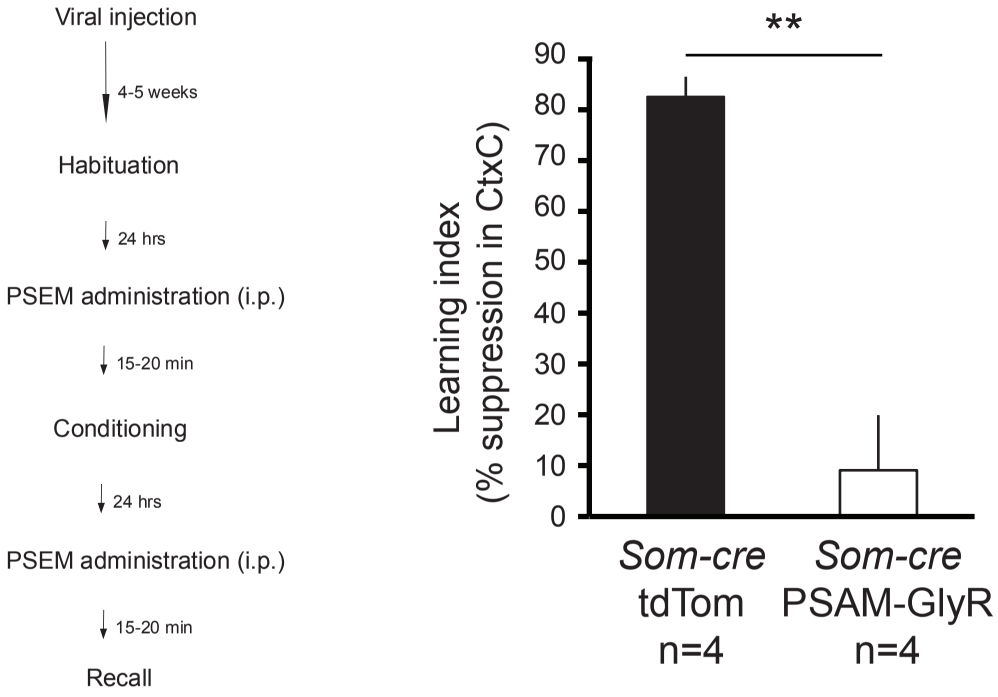

Supplementary Figure 4
Lovett-Barron et al.

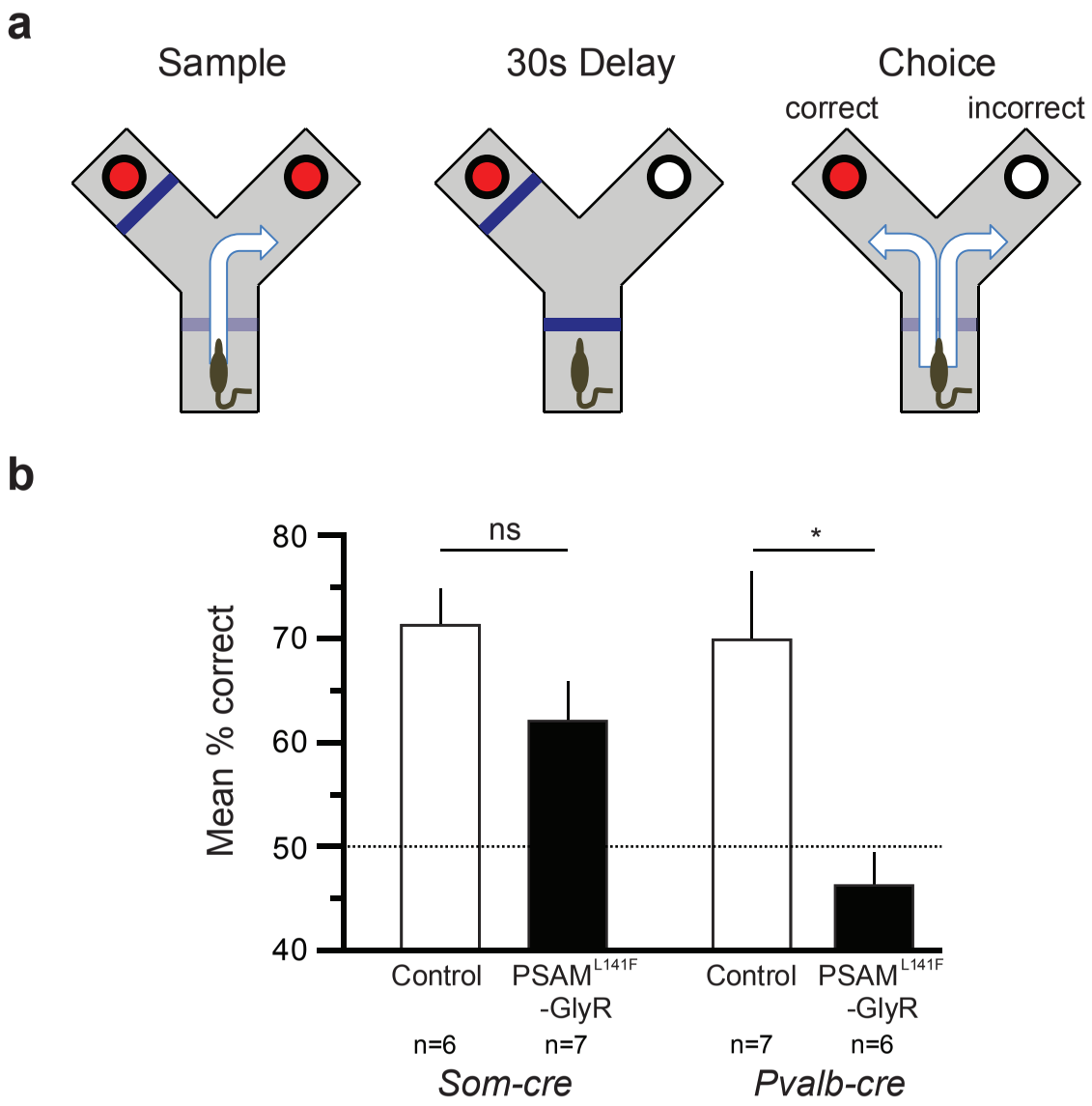

Supplementary Figure 5
Lovett-Barron et al.

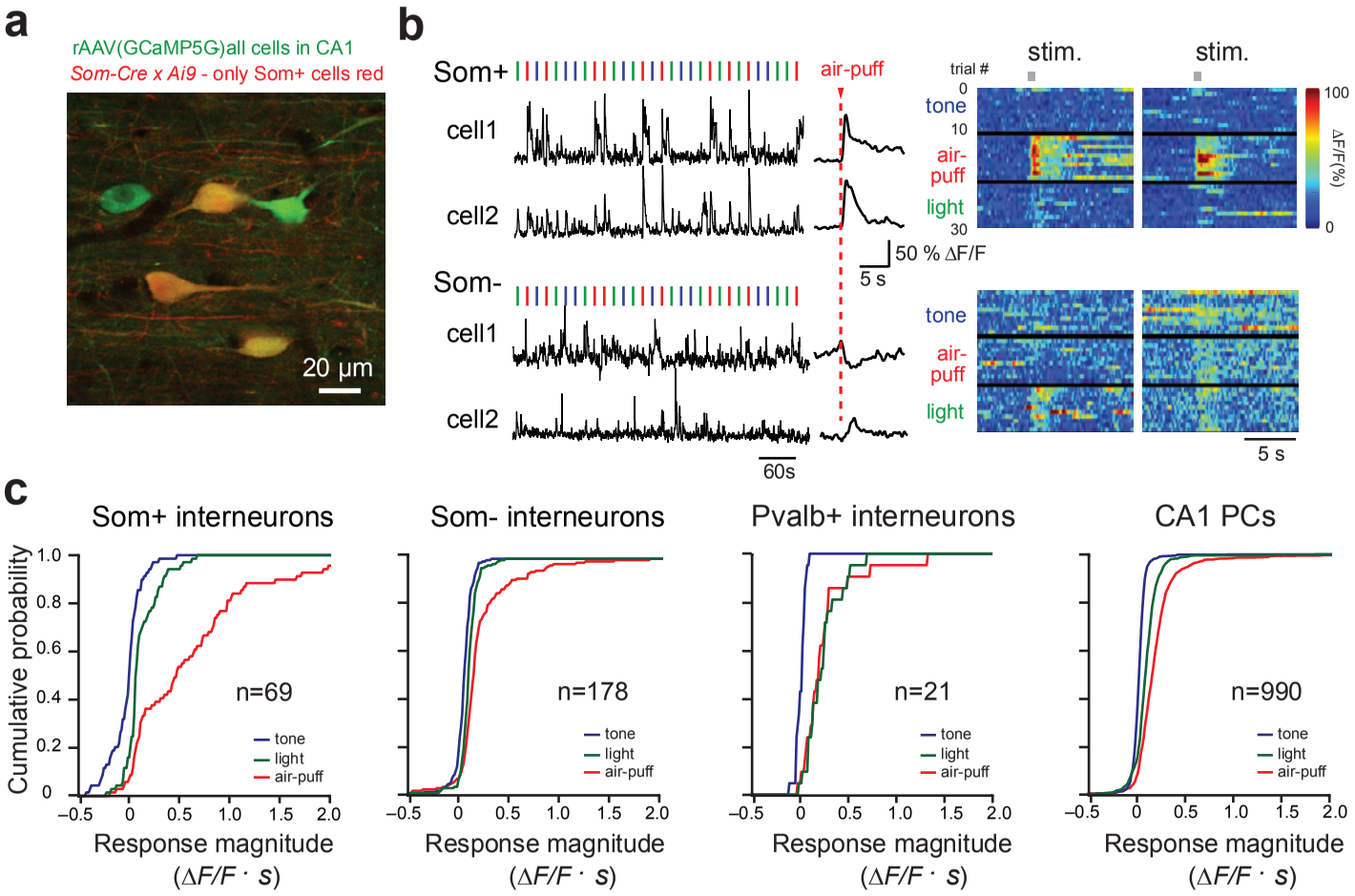

Supplementary Figure 6
Lovett-Barron et al.

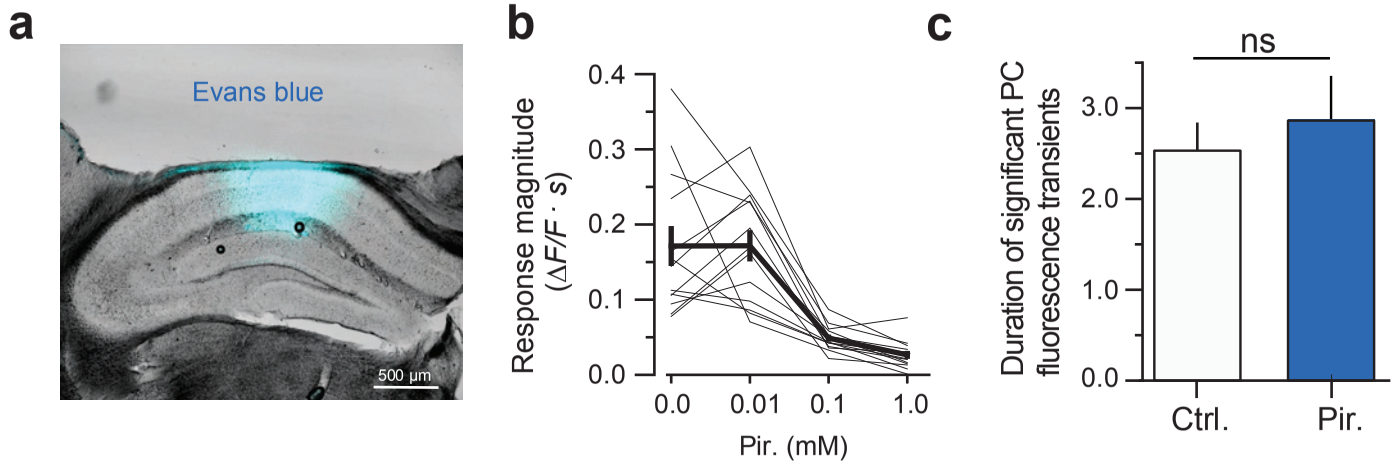

Supplementary Figure 7
Lovett-Barron et al.

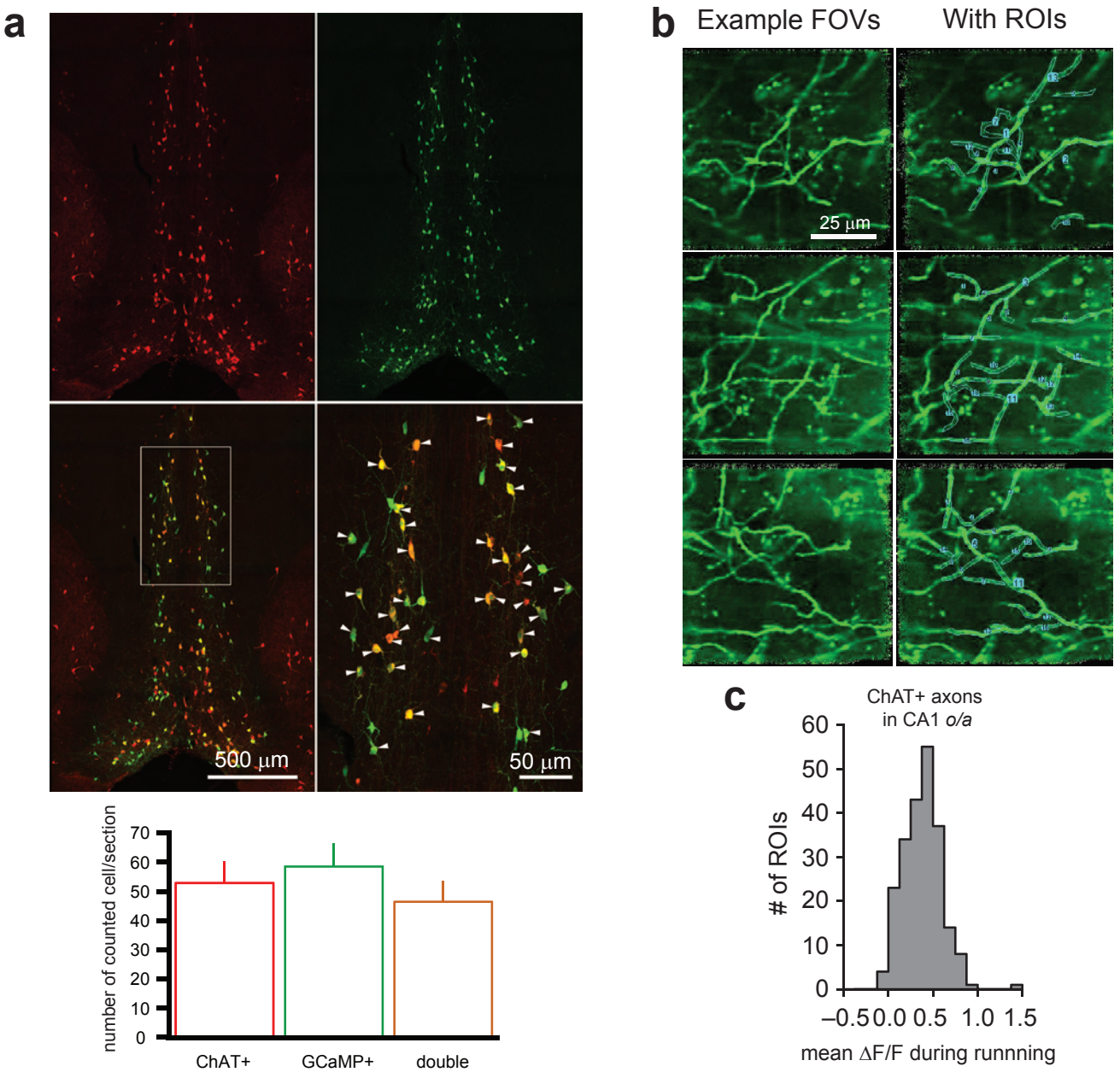

Supplementary Figure 8
Lovett-Barron et al.

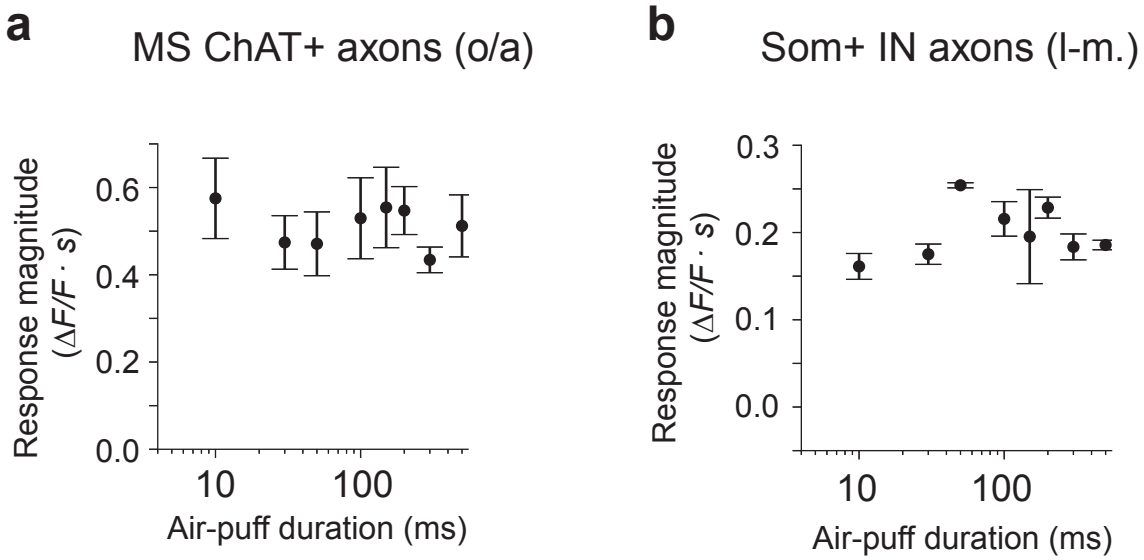

Supplementary Figure 9
Lovett-Barron et al.

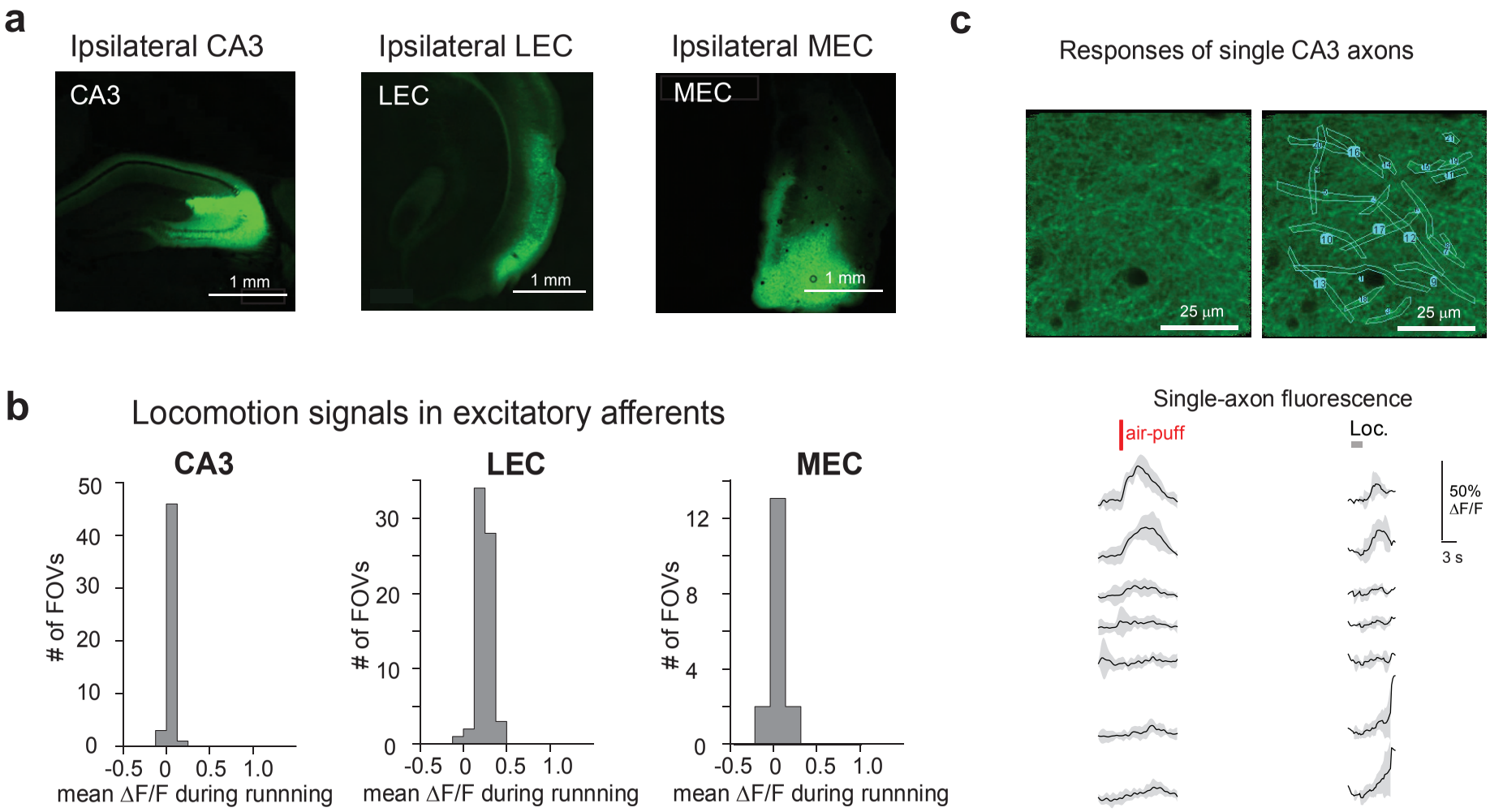

Supplementary Figure 10
Lovett-Barron et al.

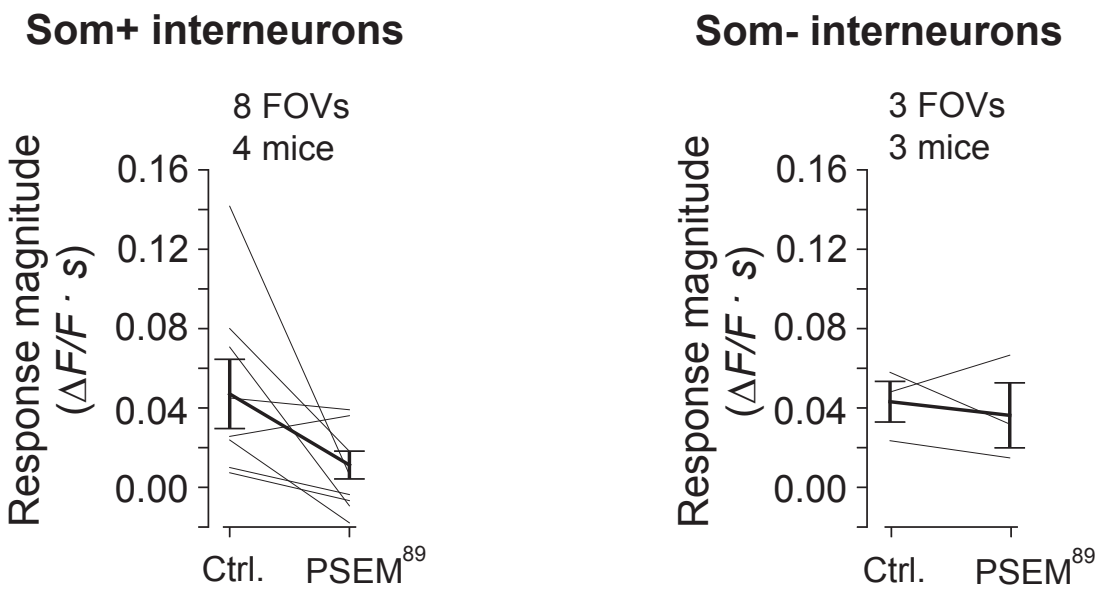

Supplementary Figure 11
Lovett-Barron et al.

a

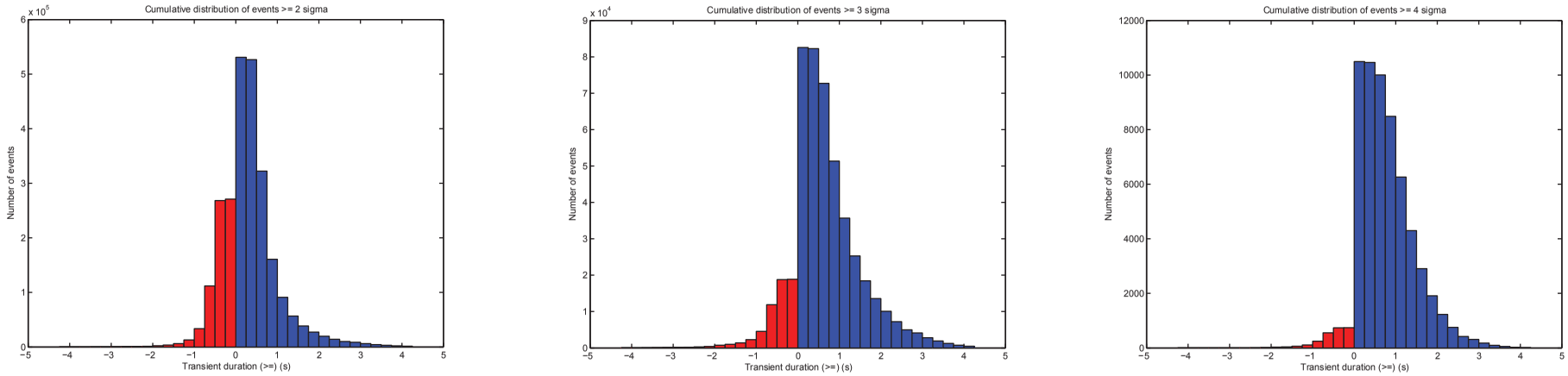

b

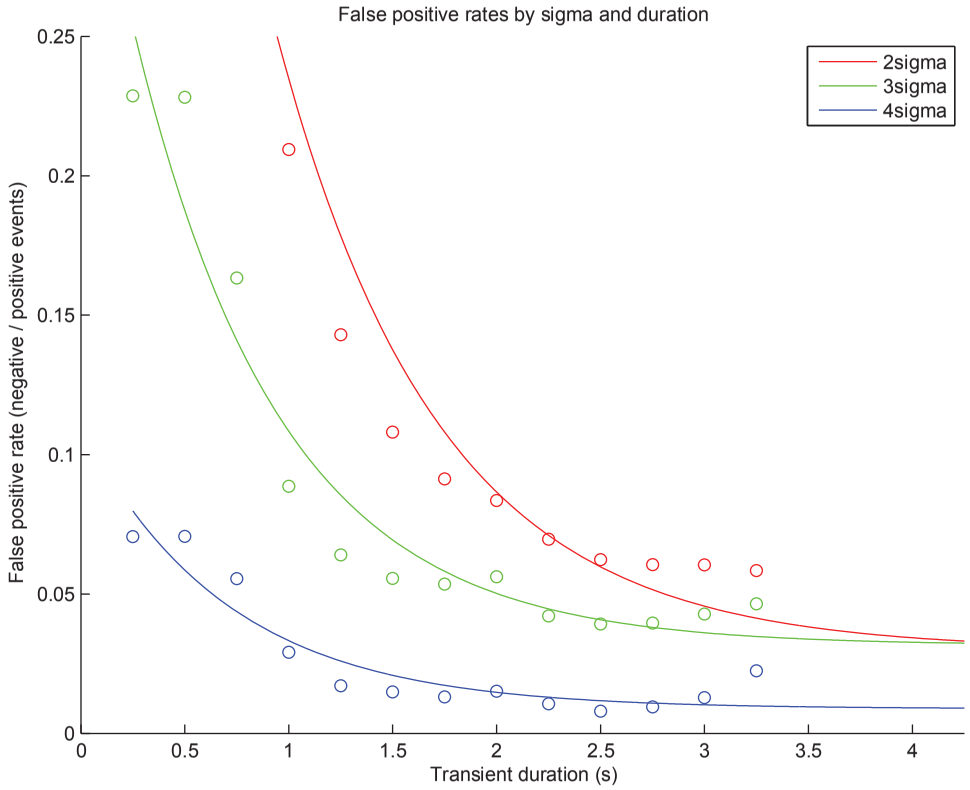

Supplementary Figure 12
Lovett-Barron et al.

a Effect of local PSEM^{89} on PCs in *Som-cre* mice not expressing PSAM^{L141F}-GlyR

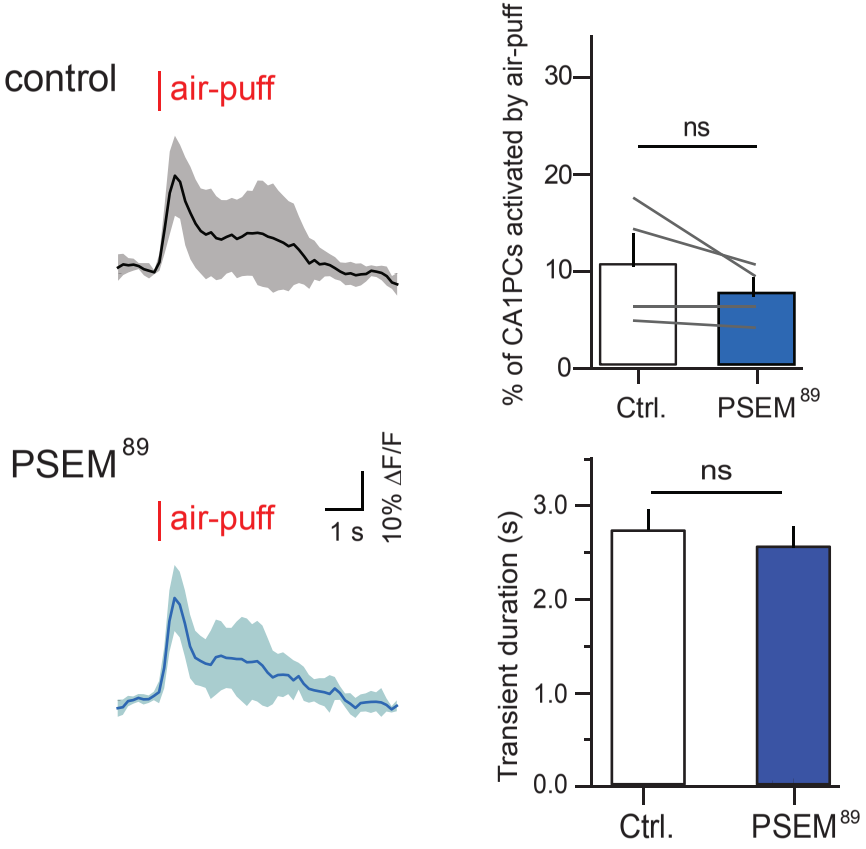

b Effect of local GABA$_A$R block (20 µM bicuculine) on PCs

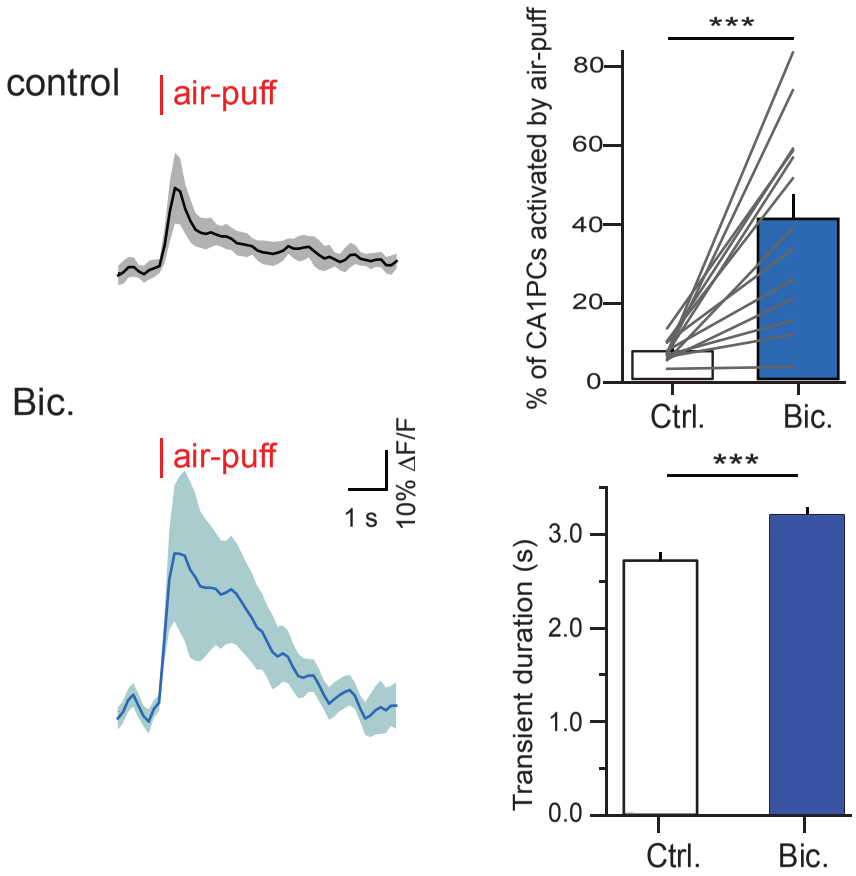

Supplementary Figure 13
Lovett-Barron et al.

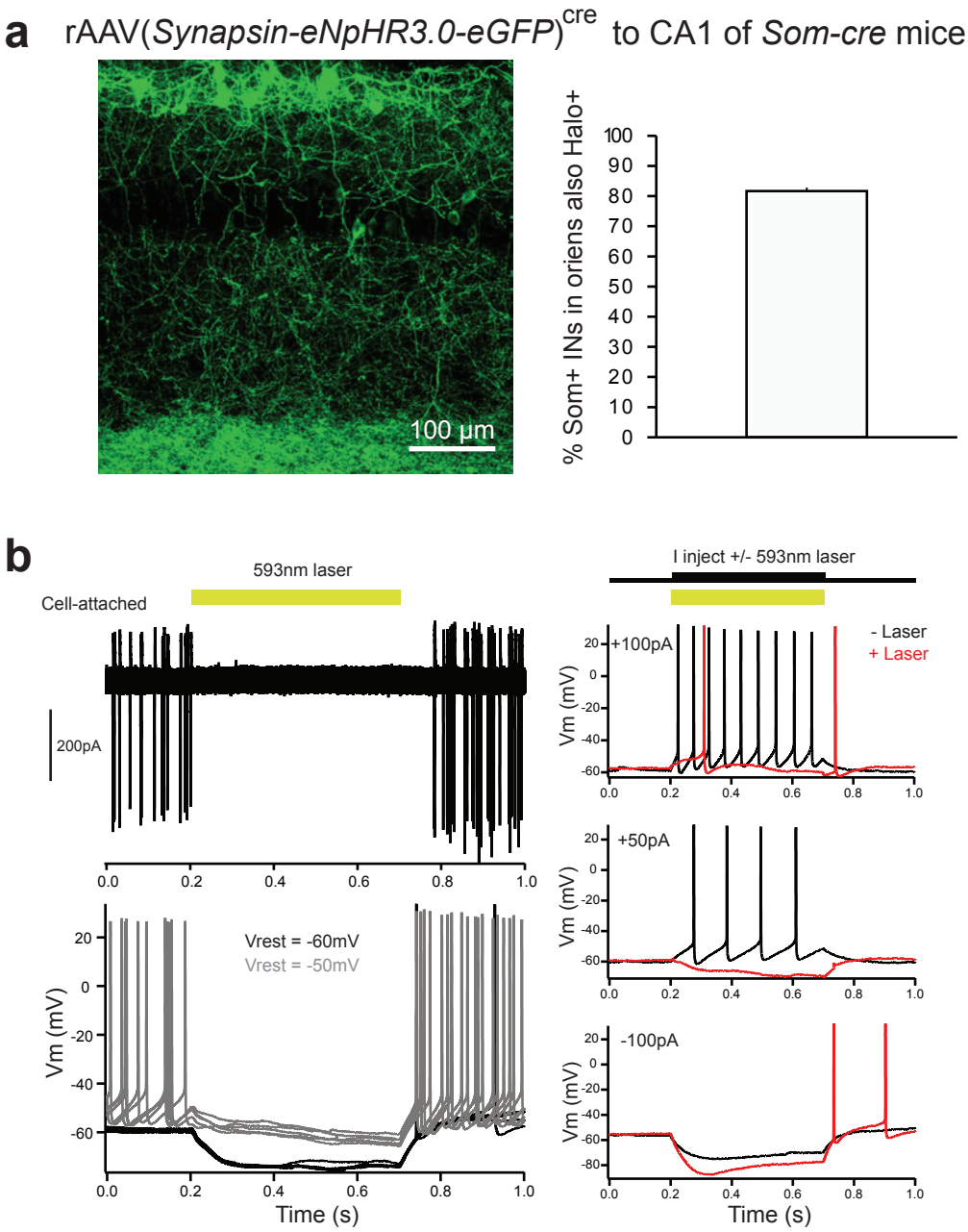

Supplementary Figure 14
Lovett-Barron et al.

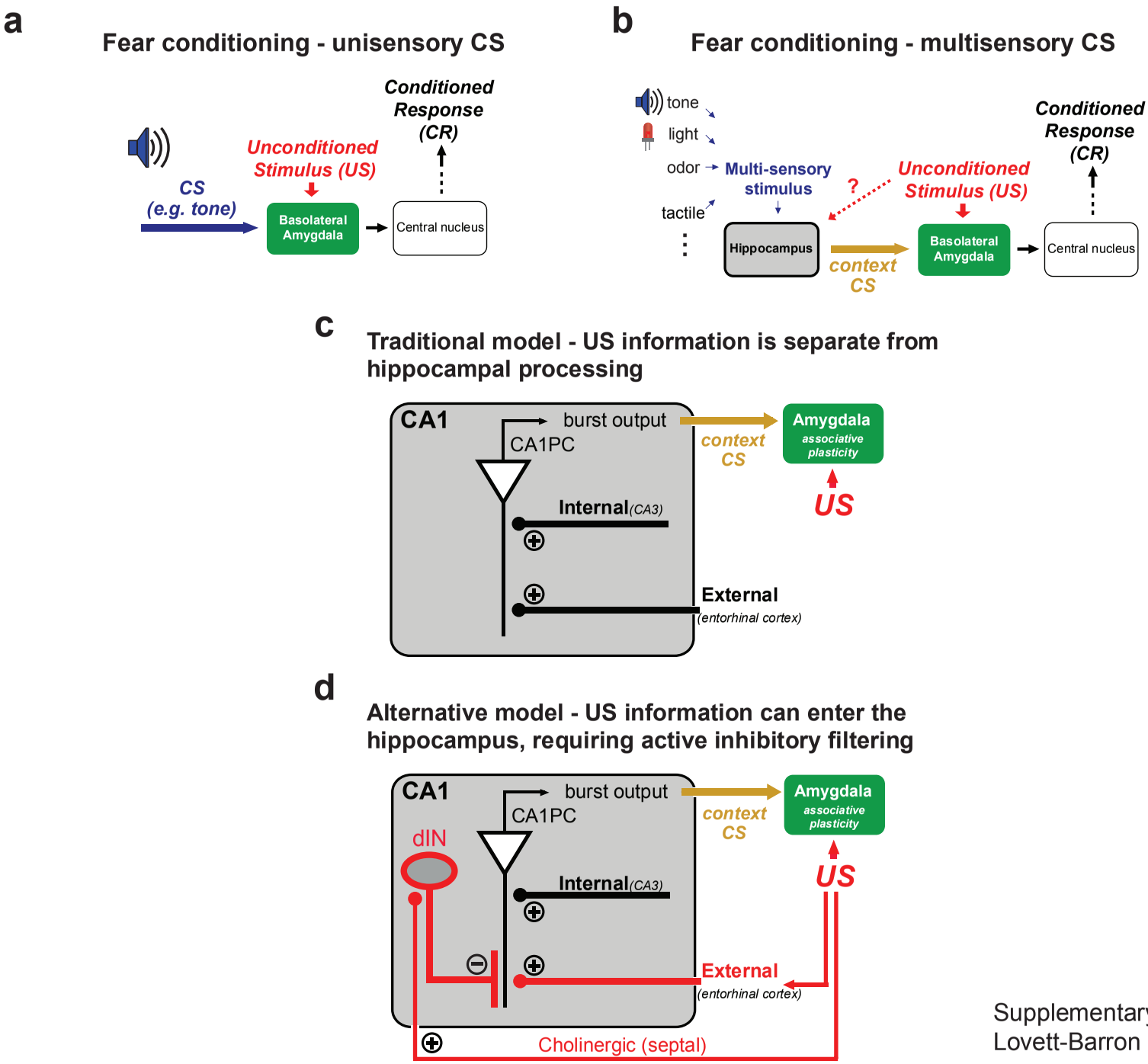

Supplementary Figure 15
Lovett-Barron et al.

References

1. M. S. Fanselow, Associative vs. topographical accounts of the immediate shock freezing deficit in rats: Implications for the response selection rules governing species specific defensive reactions. *Learn*. *Motiv*. **17**, 16–39 (1986). doi:10.1016/0023-9690(86)90018-4

2. M. S. Fanselow, Factors governing one trial contextual conditioning. *Anim*. *Learn*. *Behav*. **18**, 264–270 (1990). doi:10.3758/BF03205285

3. S. Maren, Neurobiology of Pavlovian fear conditioning. *Annu*. *Rev*. *Neurosci*. **24**, 897–931 (2001). doi:10.1146/annurev.neuro.24.1.897 Medline

4. J. W. Rudy, N. C. Huff, P. Matus-Amat, Understanding contextual fear conditioning: insights from a two-process model. *Neurosci*. *Biobehav*. *Rev*. **28**, 675–685 (2004). doi:10.1016/j.neubiorev.2004.09.004 Medline

5. M. S. Fanselow, A. M. Poulos, The neuroscience of mammalian associative learning. *Annu*. *Rev*. *Psychol*. **56**, 207–234 (2005). doi:10.1146/annurev.psych.56.091103.070213 Medline

6. J. J. Kim, M. S. Fanselow, Modality-specific retrograde amnesia of fear. *Science* **256**, 675–677 (1992). doi:10.1126/science.1585183 Medline

7. R. G. Phillips, J. E. LeDoux, Differential contribution of amygdala and hippocampus to cued and contextual fear conditioning. *Behav*. *Neurosci*. **106**, 274–285 (1992). doi:10.1037/0735-7044.106.2.274 Medline

8. S. L. Young, D. L. Bohenek, M. S. Fanselow, NMDA processes mediate anterograde amnesia of contextual fear conditioning induced by hippocampal damage: immunization against amnesia by context preexposure. *Behav*. *Neurosci*. **108**, 19–29 (1994). doi:10.1037/0735-7044.108.1.19 Medline

9. S. Maren, M. S. Fanselow, Synaptic plasticity in the basolateral amygdala induced by hippocampal formation stimulation in vivo. *J*. *Neurosci*. **15**, 7548–7564 (1995). Medline

10. P. W. Frankland, S. A. Josselyn, S. G. Anagnostaras, J. H. Kogan, E. Takahashi, A. J. Silva, Consolidation of CS and US representations in associative fear conditioning. *Hippocampus* **14**, 557–569 (2004). doi:10.1002/hipo.10208 Medline

11. M. S. Fanselow, J. P. DeCola, S. L. Young, Mechanisms responsible for reduced contextual conditioning with massed unsignaled unconditional stimuli. *J*. *Exp*. *Psychol*. *Anim*. *Behav*. *Process*. **19**, 121–137 (1993). doi:10.1037/0097-7403.19.2.121 Medline

12. P. Sah, E. S. Faber, M. Lopez De Armentia, J. Power, The amygdaloid complex: anatomy and physiology. *Physiol*. *Rev*. **83**, 803–834 (2003). Medline

13. O. J. Ahmed, M. R. Mehta, The hippocampal rate code: Anatomy, physiology and theory. *Trends Neurosci*. **32**, 329–338 (2009). doi:10.1016/j.tins.2009.01.009 Medline

14. R. P. Kesner, Behavioral functions of the CA3 subregion of the hippocampus. *Learn*. *Mem*. **14**, 771–781 (2007). doi:10.1101/lm.688207 Medline

15. S. Maren, M. S. Fanselow, Electrolytic lesions of the fimbria/fornix, dorsal hippocampus, or entorhinal cortex produce anterograde deficits in contextual fear conditioning in rats. *Neurobiol*. *Learn*. *Mem*. **67**, 142–149 (1997). doi:10.1006/nlme.1996.3752 Medline

16. N. L. Golding, N. P. Staff, N. Spruston, Dendritic spikes as a mechanism for cooperative long-term potentiation. *Nature* **418**, 326–331 (2002). doi:10.1038/nature00854 Medline

17. J. T. Dudman, D. Tsay, S. A. Siegelbaum, A role for synaptic inputs at distal dendrites: instructive signals for hippocampal long-term plasticity. *Neuron* **56**, 866–879 (2007). doi:10.1016/j.neuron.2007.10.020 Medline

18. H. Takahashi, J. C. Magee, Pathway interactions and synaptic plasticity in the dendritic tuft regions of CA1 pyramidal neurons. *Neuron* **62**, 102–111 (2009). doi:10.1016/j.neuron.2009.03.007 Medline

19. M. W. Jones, M. A. Wilson, Theta rhythms coordinate hippocampal-prefrontal interactions in a spatial memory task. *PLoS Biol*. **3**, e402 (2005). doi:10.1371/journal.pbio.0030402 Medline

20. K. D. Harris, H. Hirase, X. Leinekugel, D. A. Henze, G. Buzsáki, Temporal interaction between single spikes and complex spike bursts in hippocampal pyramidal cells. *Neuron* **32**, 141–149 (2001). doi:10.1016/S0896-6273(01)00447-0 Medline

21. W. Xu, W. Morishita, P. S. Buckmaster, Z. P. Pang, R. C. Malenka, T. C. Südhof, Distinct neuronal coding schemes in memory revealed by selective erasure of fast synchronous synaptic transmission. *Neuron* **73**, 990–1001 (2012). doi:10.1016/j.neuron.2011.12.036 Medline

22. T. F. Freund, G. Buzsáki, Interneurons of the hippocampus. *Hippocampus* **6**, 347–470 (1996). doi:10.1002/(SICI)1098-1063(1996)6:4<347::AID-HIPO1>3.0.CO;2-I Medline

23. T. Klausberger, P. Somogyi, Neuronal diversity and temporal dynamics: The unity of hippocampal circuit operations. *Science* **321**, 53–57 (2008). doi:10.1126/science.1149381 Medline

24. A. Losonczy, B. V. Zemelman, A. Vaziri, J. C. Magee, Network mechanisms of theta related neuronal activity in hippocampal CA1 pyramidal neurons. *Nat*. *Neurosci*. **13**, 967–972 (2010). doi:10.1038/nn.2597 Medline

25. M. Lovett-Barron, G. F. Turi, P. Kaifosh, P. H. Lee, F. Bolze, X. H. Sun, J. F. Nicoud, B. V. Zemelman, S. M. Sternson, A. Losonczy, Regulation of neuronal input transformations by tunable dendritic inhibition. *Nat*. *Neurosci*. **15**, 423–430, S1–S3 (2012). doi:10.1038/nn.3024 Medline

26. S. Royer, B. V. Zemelman, A. Losonczy, J. Kim, F. Chance, J. C. Magee, G. Buzsáki, Control of timing, rate and bursts of hippocampal place cells by dendritic and somatic inhibition. *Nat*. *Neurosci*. **15**, 769–775 (2012). doi:10.1038/nn.3077 Medline

27. W. J. Mahoney, J. J. B. Ayres, One-trial simultaneous and backward fear conditioning as reflected in conditioned suppression of licking in rats. *Anim*. *Learn*. *Behav*. **4**, 357–362 (1976). doi:10.3758/BF03214421

28. M. E. Bouton, R. C. Bolles, Conditioned fear assessed by freezing and by the suppression of three different baselines. *Anim*. *Learn*. *Behav*. **8**, 429–434 (1980). doi:10.3758/BF03199629

29. P. Kaifosh, M. Lovett-Barron, G. F. Turi, T. R. Reardon, A. Losonczy, Septo-hippocampal GABAergic signaling across multiple modalities in awake mice. *Nat*. *Neurosci*. **16**, 1182–1184 (2013). doi:10.1038/nn.3482 Medline

30. C. J. Magnus, P. H. Lee, D. Atasoy, H. H. Su, L. L. Looger, S. M. Sternson, Chemical and genetic engineering of selective ion channel-ligand interactions. *Science* **333**, 1292–1296 (2011). doi:10.1126/science.1206606 Medline

31. S. G. Anagnostaras, G. D. Gale, M. S. Fanselow, Hippocampus and contextual fear conditioning: recent controversies and advances. *Hippocampus* **11**, 8–17 (2001). doi:10.1002/1098-1063(2001)11:1<8::AID-HIPO1015>3.0.CO;2-7 Medline

32. I. Goshen, M. Brodsky, R. Prakash, J. Wallace, V. Gradinaru, C. Ramakrishnan, K. Deisseroth, Dynamics of retrieval strategies for remote memories. *Cell* **147**, 678–689 (2011). doi:10.1016/j.cell.2011.09.033 Medline

33. A. J. Murray, J. F. Sauer, G. Riedel, C. McClure, L. Ansel, L. Cheyne, M. Bartos, W. Wisden, P. Wulff, Parvalbumin-positive CA1 interneurons are required for spatial working but not for reference memory. *Nat*. *Neurosci*. **14**, 297–299 (2011). doi:10.1038/nn.2751 Medline

34. J. Akerboom, T. W. Chen, T. J. Wardill, L. Tian, J. S. Marvin, S. Mutlu, N. C. Calderón, F. Esposti, B. G. Borghuis, X. R. Sun, A. Gordus, M. B. Orger, R. Portugues, F. Engert, J. J. Macklin, A. Filosa, A. Aggarwal, R. A. Kerr, R. Takagi, S. Kracun, E. Shigetomi, B. S. Khakh, H. Baier, L. Lagnado, S. S. Wang, C. I. Bargmann, B. E. Kimmel, V. Jayaraman, K. Svoboda, D. S. Kim, E. R. Schreiter, L. L. Looger, Optimization of a GCaMP calcium indicator for neural activity imaging. *J*. *Neurosci*. **32**, 13819–13840 (2012). doi:10.1523/JNEUROSCI.2601-12.2012 Medline

35. D. A. Dombeck, C. D. Harvey, L. Tian, L. L. Looger, D. W. Tank, Functional imaging of hippocampal place cells at cellular resolution during virtual navigation. *Nat*. *Neurosci*. **13**, 1433–1440 (2010). doi:10.1038/nn.2648 Medline

36. D. A. Dombeck, A. N. Khabbaz, F. Collman, T. L. Adelman, D. W. Tank, Imaging large-scale neural activity with cellular resolution in awake, mobile mice. *Neuron* **56**, 43–57 (2007). doi:10.1016/j.neuron.2007.08.003 Medline

37. O. Herreras, J. M. Solís, M. D. Muñoz, R. Martín del Río, J. Lerma, Sensory modulation of hippocampal transmission. I. Opposite effects on CA1 and dentate gyrus synapsis. *Brain Res*. **461**, 290–302 (1988). doi:10.1016/0006-8993(88)90259-4 Medline

38. S. Khanna, Dorsal hippocampus field CA1 pyramidal cell responses to a persistent versus an acute nociceptive stimulus and their septal modulation. *Neuroscience* **77**, 713–721 (1997). doi:10.1016/S0306-4522(96)00456-3 Medline

39. M. Funahashi, Y. F. He, T. Sugimoto, R. Matsuo, Noxious tooth pulp stimulation suppresses c-fos expression in the rat hippocampal formation. *Brain Res*. **827**, 215–220 (1999). doi:10.1016/S0006-8993(99)01250-0 Medline

40. O. S. Vinogradova, Hippocampus as comparator: Role of the two input and two output systems of the hippocampus in selection and registration of information. *Hippocampus* **11**, 578–598 (2001). doi:10.1002/hipo.1073 Medline

41. J. J. Lawrence, J. M. Statland, Z. M. Grinspan, C. J. McBain, Cell type-specific dependence of muscarinic signalling in mouse hippocampal stratum oriens interneurones. *J*. *Physiol*. **570**, 595–610 (2006). doi:10.1113/jphysiol.2005.100875 Medline

42. R. N. Leão, S. Mikulovic, K. E. Leão, H. Munguba, H. Gezelius, A. Enjin, K. Patra, A. Eriksson, L. M. Loew, A. B. Tort, K. Kullander, OLM interneurons differentially modulate CA3 and entorhinal inputs to hippocampal CA1 neurons. *Nat*. *Neurosci*. **15**, 1524–1530 (2012). doi:10.1038/nn.3235 Medline

43. S. W. Miller, P. M. Groves, Sensory evoked neuronal activity in the hippocampus before and after lesions of the medial septal nuclei. *Physiol*. *Behav*. **18**, 141–146 (1977). doi:10.1016/0031-9384(77)90106-8 Medline

44. O. Herreras, J. M. Solís, A. S. Herranz, R. M. del Río, J. Lerma, Sensory modulation of hippocampal transmission. II. Evidence for a cholinergic locus of inhibition in the Schaffer-CA1 synapse. *Brain Res*. **461**, 303–313 (1988). doi:10.1016/0006-8993(88)90260-0 Medline

45. F. Zheng, S. Khanna, Selective destruction of medial septal cholinergic neurons attenuates pyramidal cell suppression, but not excitation in dorsal hippocampus field CA1 induced by subcutaneous injection of formalin. *Neuroscience* **103**, 985–998 (2001). doi:10.1016/S0306-4522(01)00006-9 Medline

46. J. J. Letzkus, S. B. Wolff, E. M. Meyer, P. Tovote, J. Courtin, C. Herry, A. Lüthi, A disinhibitory microcircuit for associative fear learning in the auditory cortex. *Nature* **480**, 331–335 (2011). doi:10.1038/nature10674 Medline

47. H. Widmer, L. Ferrigan, C. H. Davies, S. R. Cobb, Evoked slow muscarinic acetylcholinergic synaptic potentials in rat hippocampal interneurons. *Hippocampus* **16**, 617–628 (2006). doi:10.1002/hipo.20191 Medline

48. G. D. Gale, S. G. Anagnostaras, M. S. Fanselow, Cholinergic modulation of pavlovian fear conditioning: effects of intrahippocampal scopolamine infusion. *Hippocampus* **11**, 371–376 (2001). doi:10.1002/hipo.1051 Medline

49. S. Dasari, A. T. Gulledge, M1 and M4 receptors modulate hippocampal pyramidal neurons. *J*. *Neurophysiol*. **105**, 779–792 (2011). doi:10.1152/jn.00686.2010 Medline

50. M. E. Hasselmo, The role of acetylcholine in learning and memory. *Curr*. *Opin*. *Neurobiol*. **16**, 710–715 (2006). doi:10.1016/j.conb.2006.09.002 Medline

51. L. Calandreau, R. Jaffard, A. Desmedt, Dissociated roles for the lateral and medial septum in elemental and contextual fear conditioning. *Learn*. *Mem*. **14**, 422–429 (2007). doi:10.1101/lm.531407 Medline

52. T.-W. Chen, T. J. Wardill, Y. Sun, S. R. Pulver, S. L. Renninger, A. Baohan, E. R. Schreiter, R. A. Kerr, M. B. Orger, V. Jayaraman, L. L. Looger, K. Svoboda, D. S. Kim, Ultrasensitive fluorescent proteins for imaging neuronal activity. *Nature* **499**, 295–300 (2013). doi:10.1038/nature12354 Medline

53. E. L. Hargreaves, G. Rao, I. Lee, J. J. Knierim, Major dissociation between medial and lateral entorhinal input to dorsal hippocampus. *Science* **308**, 1792–1794 (2005). doi:10.1126/science.1110449 Medline

54. S. J. Zhang, J. Ye, C. Miao, A. Tsao, I. Cerniauskas, D. Ledergerber, M. B. Moser, E. I. Moser, Optogenetic dissection of entorhinal-hippocampal functional connectivity. *Science* **340**, 1232627 (2013). doi:10.1126/science.1232627 Medline

55. L. Palmer, M. Murayama, M. Larkum, Inhibitory regulation of dendritic activity in vivo. *Frontiers in Neural Circuits* **6**, 26 (2012). doi:10.3389/fncir.2012.00026 Medline

56. F. Zhang, L. P. Wang, M. Brauner, J. F. Liewald, K. Kay, N. Watzke, P. G. Wood, E. Bamberg, G. Nagel, A. Gottschalk, K. Deisseroth, Multimodal fast optical interrogation of neural circuitry. *Nature* **446**, 633–639 (2007). doi:10.1038/nature05744 Medline

57. L. M. Romanski, J. E. LeDoux, Information cascade from primary auditory cortex to the amygdala: corticocortical and corticoamygdaloid projections of temporal cortex in the rat. *Cereb*. *Cortex* **3**, 515–532 (1993). doi:10.1093/cercor/3.6.515 Medline

58. E. Lanuza, K. Nader, J. E. Ledoux, Unconditioned stimulus pathways to the amygdala: effects of posterior thalamic and cortical lesions on fear conditioning. *Neuroscience* **125**, 305–315 (2004). doi:10.1016/j.neuroscience.2003.12.034 Medline

59. J. Brankačk, G. Buzsáki, Hippocampal responses evoked by tooth pulp and acoustic stimulation: depth profiles and effect of behavior. *Brain Res*. **378**, 303–314 (1986). doi:10.1016/0006-8993(86)90933-9 Medline

60. R. D. Burwell, D. G. Amaral, Cortical afferents of the perirhinal, postrhinal, and entorhinal cortices of the rat. *J*. *Comp*. *Neurol*. **398**, 179–205 (1998). doi:10.1002/(SICI)1096-9861(19980824)398:2<179::AID-CNE3>3.0.CO;2-Y Medline

61. S. Melzer, M. Michael, A. Caputi, M. Eliava, E. C. Fuchs, M. A. Whittington, H. Monyer, Long-range-projecting GABAergic neurons modulate inhibition in hippocampus and entorhinal cortex. *Science* **335**, 1506–1510 (2012). doi:10.1126/science.1217139 Medline

62. M. A. Moita, S. Rosis, Y. Zhou, J. E. LeDoux, H. T. Blair, Putting fear in its place: remapping of hippocampal place cells during fear conditioning. *J*. *Neurosci*. **24**, 7015–7023 (2004). doi:10.1523/JNEUROSCI.5492-03.2004 Medline

63. C. I. Bargmann, Beyond the connectome: How neuromodulators shape neural circuits. *Bioessays* **34**, 458–465 (2012) Supplementary References. doi:10.1002/bies.201100185 Medline

64. C. McClure, K. L. Cole, P. Wulff, M. Klugmann, A. J. Murray, Production and titering of recombinant adeno-associated viral vectors. *J*. *Vis*. *Exp*. **57**, e3348 (2011). 10.3791/3348 Medline

65. M. A. Kheirbek, L. J. Drew, N. S. Burghardt, D. O. Costantini, L. Tannenholz, S. E. Ahmari, H. Zeng, A. A. Fenton, R. Hen, Differential control of learning and anxiety along the dorsoventral axis of the dentate gyrus. *Neuron* **77**, 955–968 (2013). doi:10.1016/j.neuron.2012.12.038 Medline

66. R. M. J. Deacon, J. N. P. Rawlins, T-maze alternation in the rodent. *Nat*. *Protoc*. **1**, 7–12 (2006). doi:10.1038/nprot.2006.2 Medline